

## The Globular Cluster System of the Virgo Cluster Ultradiffuse Galaxy VCC 615

J. CHRISTOPHER MIHOS,<sup>1</sup> PATRICK R. DURRELL,<sup>2</sup> ELISA TOLOBA,<sup>3</sup> ERIC W. PENG,<sup>4</sup> SUNGSOON LIM,<sup>5</sup> PATRICK CÔTÉ,<sup>6</sup>  
PURAGRA GUHATHAKURTA,<sup>7</sup> AND LAURA FERRARESE<sup>6</sup>

<sup>1</sup>*Department of Astronomy, Case Western Reserve University, Cleveland OH 44106, USA*

<sup>2</sup>*Department of Physics, Astronomy, Geophysics and Environmental Sciences, Youngstown State University, Youngstown, OH 44555 USA*

<sup>3</sup>*Department of Physics and Astronomy, University of the Pacific, Stockton, CA 95211, USA*

<sup>4</sup>*NOIRLab, 950 North Cherry Ave, Tucson, AZ, 85719, USA*

<sup>5</sup>*Department of Astronomy, Yonsei University, 50 Yonsei-ro Seodaemun-gu, Seoul, 03722, Republic of Korea*

<sup>6</sup>*National Research Council of Canada, Herzberg Astronomy and Astrophysics Program, Victoria, BC V9E 2E7, Canada*

<sup>7</sup>*UCO/Lick Observatory, University of California Santa Cruz, Santa Cruz, CA 95064, USA*

### ABSTRACT

We use *Hubble Space Telescope* imaging to study the globular cluster system of the Virgo Cluster ultradiffuse galaxy (UDG) VCC 615. We select globular cluster candidates through a combination of size and color, while simultaneously rejecting contamination from background galaxies that would be unresolved in ground-based imaging. Our sample of globular cluster candidates is essentially complete down to a limiting magnitude of  $F814W=24.0$ ,  $\approx 90\%$  down the globular cluster luminosity function. We estimate a total globular cluster population for VCC 615 of  $N_{GC} = 25.1_{-5.4}^{+6.5}$ , resulting in a specific frequency of  $S_N = 55.5_{-12.0}^{+14.5}$ , quite high compared to normal galaxies of similar luminosity, but consistent with the large specific frequencies found in some other UDGs. The abundant cluster population suggests the galaxy is enshrouded by a massive dark halo, consistent with previous dynamical mass estimates using globular cluster kinematics. While the peak of the globular cluster luminosity function appears slightly brighter than expected (by  $\approx 0.3$ – $0.5$  mag), this difference is comparable to the 0.3 mag uncertainty in the measurement, and we see no sign of an extremely luminous population of clusters similar to those detected in the UDGs NGC1054-DF2 and -DF4. However, we do find a relatively high fraction ( $32_{-4}^{+5}\%$ ) of large clusters with half-light radii  $R_h > 9$  pc. The galaxy’s offset nucleus appears photometrically distinct from the globular clusters, and is more akin to ultracompact dwarfs (UCDs) in Virgo. Over time, VCC615’s already diffuse stellar body may be further stripped by cluster tides, leaving the nucleus intact to form a new Virgo UCD.

*Keywords:* Globular Clusters — Dwarf Galaxies — Galaxy clusters — Galaxy evolution — Low Surface Brightness Galaxies

### 1. INTRODUCTION

The nature of ultradiffuse galaxies (UDGs) continues to pose complicated questions about the formation and evolution of galaxies. UDGs are large and extremely diffuse galaxies first identified in dense galaxy clusters (Sandage & Binggeli 1984; Binggeli et al. 1987; van Dokkum et al. 2015; Mihos et al. 2015), but are now known to populate a variety of environments, including field and group environments (Barbosa et al. 2020; Marleau et al. 2021; Zaritsky et al. 2023). These objects show a wide range of properties, from the “red and dead” gas-poor UDGs typically found in denser environments to those with bluer colors and surprisingly high gas fractions (Cannon et al. 2015; Leisman et al. 2017;

Mihos et al. 2018). This diversity in the UDG population has led to a variety of proposed formation scenarios. Some invoke processes that are intrinsic to the galaxy upon formation, such as having a halo of high spin or low concentration (Amorisco & Loeb 2016; Benavides et al. 2023), a truncated star formation history (Peng & Lim 2016; van Dokkum et al. 2015, 2016; Janssens et al. 2022), or having experienced overly-disruptive feedback from bursty star formation (Di Cintio et al. 2017). Other scenarios rely on subsequent evolutionary processes such as tidal stripping and heating (Moore et al. 1996; Liao et al. 2019; Carleton et al. 2019) to transform otherwise normal galaxies into UDGs at later times. These processes are not mutually exclusive, and both intrinsic

sic formation scenarios and subsequent evolution can in principle combine to shape UDGs in a wide variety of ways. In fact, these processes may provide an evolutionary link between UDGs and ultracompact dwarf galaxies (UCDs) in dense clusters, if nucleated UDGs are completely disrupted by cluster tides leaving only their compact nuclei behind (e.g., Bekki et al. 2003; Pfeffer & Baumgardt 2013; Liu et al. 2015, 2020; Janssens et al. 2019; Wang et al. 2023).

The dark matter content of UDGs is of particular importance in disentangling these different scenarios — do UDGs have low mass dwarf-like halos, or are they cocooned in massive dark halos characteristic of more luminous galaxies? Dynamical mass estimates of UDGs show a range of possibilities. Some UDGs have very high mass-to-light ratios (Beasley et al. 2016; Toloba et al. 2018; Forbes et al. 2021; Toloba et al. 2023), indicating the presence of an overly-massive dark halo, while other UDGs have much lower dynamical mass-to-light ratios (van Dokkum et al. 2019; Chilingarian et al. 2019; Toloba et al. 2023), including some objects in which the stellar mass dominates to total mass (van Dokkum et al. 2018a; Danieli et al. 2019; Toloba et al. 2023). Here again, the diversity of dynamical properties points to UDGs being a heterogeneous class of objects arising from multiple formation scenarios.

Into this picture, globular clusters provide important and complementary information about the properties of UDGs. UDGs have a wide range of globular cluster specific frequencies ( $S_N = N_{GC}10^{0.4(M_V+15)}$ ; Harris & van den Bergh 1981); some have abundant cluster systems (Peng & Lim 2016; van Dokkum et al. 2017; Lim et al. 2018; Müller et al. 2021; Saifollahi et al. 2021; Danieli et al. 2022; Fielder et al. 2023; Forbes & Gannon 2024), while others show sparser cluster populations or sometimes no clusters at all (Amorisco et al. 2018; Prole et al. 2019; Lim et al. 2020; Forbes et al. 2020; Marleau et al. 2024). In the normal galaxy population, multiple studies have shown a correlation between the number of globular clusters ( $N_{GC}$ ) or total mass of globular clusters ( $M_{GC}$ ) in a galaxy and its total dynamical mass (e.g., Blakeslee et al. 1997; Peng et al. 2008; Spitler & Forbes 2009; Georgiev et al. 2010; Harris et al. 2013; Hudson et al. 2014; Harris et al. 2017; Burkert & Forbes 2020; Zaritsky 2022). As shown by those studies, this correlation holds over a wide range of galaxy mass, from dwarf galaxies to massive ellipticals and cD galaxies. If UDGs also follow these relationships, the globular cluster-rich UDGs are much more dark-matter dominated than their globular cluster-poor counterparts, again arguing for a variety of formation channels for UDGs. However, whether these differences in cluster populations truly trace differences

in dark matter content remains unclear; in objects where both dynamical masses and globular cluster counts are available, these two mass estimates are sometimes discrepant (e.g., van Dokkum et al. 2019). Nonetheless, if the connection between globular clusters and dark halo mass can be shown universally to hold for UDGs, it provides an opportunity to estimate UDG halo masses through imaging alone, without the need for resource-intensive kinematic studies.

However, several factors complicate the study of globular clusters in these diffuse galaxies, particularly in ground-based imaging which often suffer from significant incompleteness and contamination effects. For example, at the distance of Virgo ( $d=16.5$  Mpc Mei et al. 2007; Cantiello et al. 2024), ground based imaging only reaches the upper half of the globular cluster luminosity function (GCLF), while also being subject to significant contamination both from foreground Milky Way stars and unresolved background galaxies. The large statistical corrections for these effects, coupled with the low total  $N_{GC}$  values in UDGs (as opposed to their luminosity-normalized specific frequency  $S_N$ ) leads to significant uncertainties in deriving the total globular cluster population of UDGs from the observed counts. For example, in the well-studied UDG DF44, estimates of the total globular cluster count have varied by factors of 4–5 between different studies (van Dokkum et al. 2016, 2017; Saifollahi et al. 2021, see also Forbes & Gannon 2024). Furthermore, there is growing evidence that the cluster populations in UDGs may show systematic differences from those of normal galaxies: some UDGs have overly-luminous globular clusters (van Dokkum et al. 2018a; Shen et al. 2021a; Janssens et al. 2022), or globular cluster systems with abnormally low scatter in color (van Dokkum et al. 2022; Janssens et al. 2022). Thus, the combination of statistical uncertainty, contamination, and possible intrinsic differences clouds the use of globular clusters for studying the distances and masses of UDGs.

In this paper, we use deep *Hubble Space Telescope* imaging to study the globular cluster populations in the ultradiffuse galaxy VCC 615, located in the outskirts of the Virgo Cluster. VCC 615 (detailed in Table 1) meets the structural definition of a UDG in the analysis by Lim et al. (2020) who examined the photometric properties of galaxies in the *Next Generation Virgo Cluster Survey* galaxy sample (Ferrarese et al. 2020) and identified galaxies that were  $2.5\sigma$  outliers in a combination of size, luminosity, and surface brightness. Several arguments make VCC 615 particularly well-suited for a study of its globular cluster system. First, our previous work has pinpointed its distance using the tip of the red giant

**Table 1.** VCC 615

| Property                | Value  | Source |
|-------------------------|--|--------|
| Center (J2000)          | (12:23:04.6, +12:00:53)  | [1]    |
| $m_{g'}$                | 17.25  | [1]    |
| $R_{e,*}$               | 26.3''   | [1]    |
| $\langle\mu_g\rangle_e$ | 26.3 mag arcsec <sup>-2</sup>  | [1]    |
| Distance                | 17.7 <sup>+0.7</sup> <sub>-0.5</sub> Mpc                             | [2]    |
| $M_{g'}$                | -14.1  | [1,2]  |
| $R_{e,*}$               | 2.25 kpc   | [1,2]  |
| $v_{sys}$               | 2089 <sup>+16</sup> <sub>-15</sub> km s <sup>-1</sup>                | [3]    |
| $M_*$                   | 7.3 ± 1.1 × 10 <sup>7</sup> M <sub>⊙</sub>                           | [4]    |
| $M_{dyn,1/2}$           | 2.3 <sup>+2.8</sup> <sub>-2.2</sub> × 10 <sup>9</sup> M <sub>⊙</sub> | [3]    |

**References**— [1] Lim et al. (2020), [2] Mihos et al. (2022), [3] Toloba et al. (2023), [4] Roediger et al. (in prep)

branch (TRGB) method (Mihos et al. 2022), putting it on the far side of Virgo at  $d = 17.7^{+0.7}_{-0.5}$  Mpc, near the cluster virial radius. The low  $\approx 0.05$  mag uncertainty in the distance modulus allows us to derive accurate physical sizes and luminosities of its cluster population. Furthermore, we have well-determined estimates of both the galaxy’s stellar mass ( $M_* = 7.3 \pm 1.1 \times 10^7 M_\odot$  Roediger et al. in prep) and dynamical mass ( $M_{dyn} = 2.3^{+2.8}_{-2.2} \times 10^9 M_\odot$ , measured within the effective radius of the globular cluster system, see Toloba et al. 2023) from ground-based imaging and spectroscopy, respectively, allowing us to test the connection between its cluster system and its halo mass. Finally, using our *Hubble* imaging we can identify globular clusters via a combination of color and image concentration, while simultaneously rejecting contamination from background galaxies which would be unresolved in ground-based imaging. We use these data to construct a very clean sample of globular clusters that probe the full range of the GCLF, giving us the ability to study the cluster system of VCC 615 — both its intrinsic properties and its connection to its host galaxy — at a very high level of accuracy. Finally, we also use the data to study the galaxy’s compact nucleus, to evaluate scenarios that propose the evolution of nucleated UDGs into UCDs, driven by tidal stripping in the dense environment of the Virgo Cluster.

## 2. OBSERVATIONAL DATA AND IMAGE REDUCTION

We imaged VCC 615 using the F475W and F814W filters of the Wide Field Channel (WFC) of the Advanced

Camera for Surveys (ACS) on the *Hubble Space Telescope* as part of program GO-15258 (Cycle 25). The goal of the F814W imaging was to perform individual point source photometry (using DOLPHOT) of faint red giant branch (RGB) stars to reach below the TRGB to obtain a distance estimate to VCC 615 (see Mihos et al. 2022); these data consisted of 14×1200s exposures taken over seven orbits. The F475W imaging was much shallower, intended only to study the galaxy’s globular cluster system, and had a total exposure time of 2050s, broken into four individual exposures over a single orbit.

For the detection, photometry and characterization of globular cluster candidates in VCC 615, we created single, deep stacked images in each of the F475W and F814W filters, using the `astrodrizzle` package within `drizzlepac`. The details of the creation of the deep, stacked F814W image were presented in (Mihos et al. 2022) but we will present the salient points here. Guiding issues during the execution of the program yielded slightly elliptical point spread functions (PSFs) for most of the individual, CTE-corrected *.flc.fits* images. Of the 14 images taken, 3 were considered unusable, thus a single, drizzled stacked F814W image was created from the remaining 11 images, after first re-registering all of the images using the `tweakreg` and `tweakback` packages within `drizzlepac` to re-write the WCS for each image. The resulting image (Figure 1) has a combined exposure time of 13200s, and clearly shows the resolution of the brightest stars within VCC 615. However, the final PSF of this stacked F814W image is also slightly elongated, which may slightly reduce our ability to resolve the smallest cluster candidates in VCC 615.

The shorter exposure times for the individual F475W images resulted in reduced effects from the trailing issues seen on the F814W images. A single, deep stacked F475W image was created using the 4 re-registered CTE-corrected *.flc.fits* images, with a combined total exposure time of 2050s.

All photometry in this paper has been performed on the stacked images and has been calibrated to the VEGAmag system using the most recent ACS zeropoints and corrected for extinction using  $A_{F475W} = 0.087$  and  $A_{F814W} = 0.041$  (Schlafly & Finkbeiner 2011).

## 3. SOURCE PHOTOMETRY AND GLOBULAR CLUSTER CANDIDATE SELECTION

Before extracting globular cluster candidates from our *Hubble* imaging, we first assess the depth of the imaging and optimize the photometric selection of clusters candidates by running a set of artificial globular cluster tests, using the code `galfit` (Peng et al. 2010) to inject 100,000 artificial globular clusters into the imag-

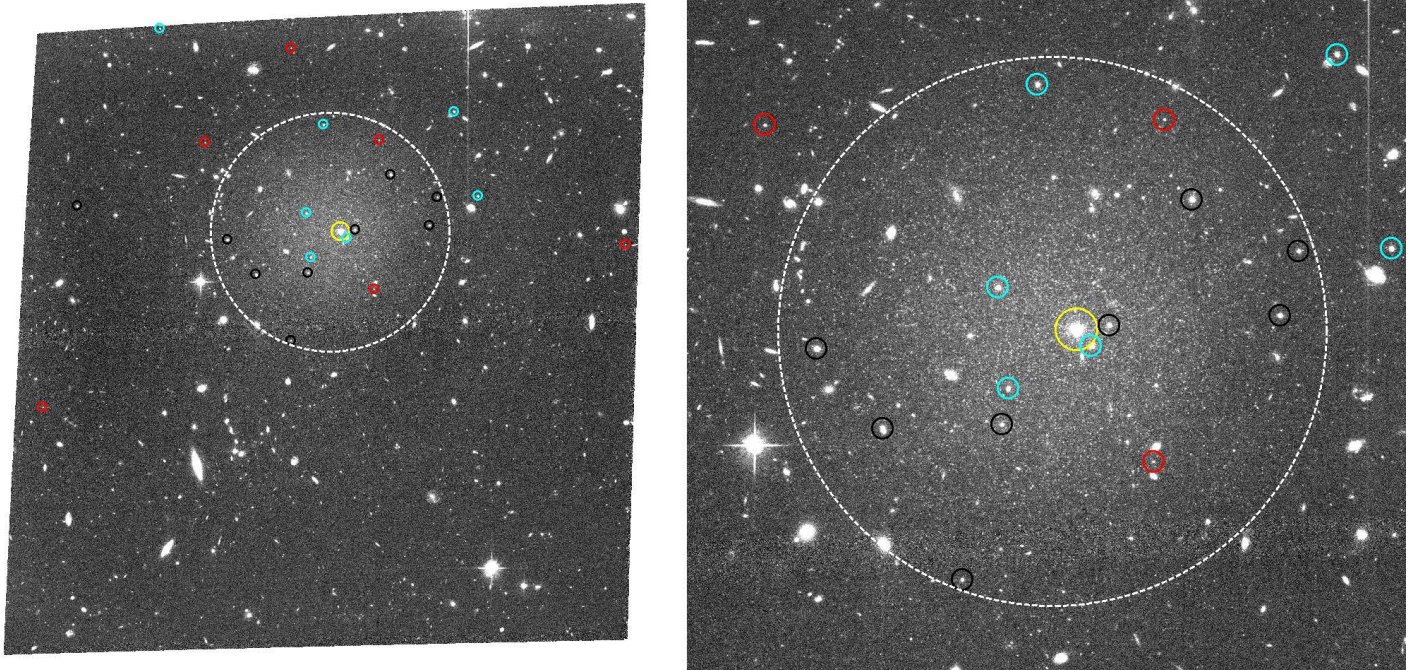


**Figure 1.** Stacked F814W ACS image of VCC 615, with a total exposure time of  $11 \times 1200$ s. The left panel shows the full  $202'' \times 202''$  ACS field of view, while the right panel is zoomed in on VCC 615. Our final globular cluster sample is marked in each panel. Red circles show unresolved candidates ( $R_h < 1.3$ pc), black circles show resolved candidates with sizes  $1.3\text{pc} < R_h < 9.0\text{pc}$ , and cyan circles show resolved candidates with sizes  $R_h > 9\text{pc}$ . VCC 615’s offset nucleus is shown with a yellow circle, and the large dotted circle shows a radius of  $1.5R_{e,*}$ . The center of the Virgo Cluster is  $1.95^\circ$  away (560 kpc in projection) to the east (upper right) of the field.

ing. The artificial globular clusters are modeled by a [King \(1966\)](#) profile, sampling evenly in absolute magnitude over the range  $-12.0 \leq M_{F814W} \leq -4.5$ , in (log) concentration over the range  $1.0 \leq \log(c) \leq 2.5$ , and in (log) physical half light radius in parsecs over the range  $-0.25 \leq \log(R_h) \leq 1.5$ . While this upper bound on size is larger than typical for Galactic globular clusters, such large clusters have been found in a variety of galactic environments (see the discussion in Section 5.1.3) and we want to search parameter space as broadly as possible to identify cluster candidates in VCC 615. At the distance of VCC 615, these parameters correspond to apparent magnitudes  $19.25 \leq F814W \leq 26.75$  and angular half light radii of  $-2.2 \leq \log(r_{e,\text{arcsec}}) \leq -0.4$ . Before injection into the imaging, we convolve the model globular clusters with the image PSF built from a set of bright stars in the ACS field.

Once injected into the images, we use the astropy-affiliated python package `photutils` ([Bradley et al. 2023](#)) to map out a local background on each image and then detect all sources  $3\sigma$  above that background. We look at the size distribution of the recovered sources, measured using the `photutils` parameter `semimajor_sigma`. The clusters are well-bounded by the range  $-0.2 \leq \log(\text{semimajor\_sigma}) \leq 1.0$  pix-

els, along with a source area of at least 9 pixels. In terms of selection depth for clusters with sizes  $R_h < 10$  pc ( $0.1''$ ), these tests show that our 50% completeness limit is  $F814W=25.1$ . For comparison, taking the M87 GCLF peak magnitude of  $\mu_{0,M87} = 22.5$  ([Peng et al. 2009](#)) and shifting it to the distance of VCC 615, the expected GCLF peak is at  $\mu_{0,VCC615} = 22.65$ , such that our imaging should detect clusters 2.5 magnitudes down the luminosity function. For more extended clusters, the completeness limit is somewhat brighter, since at fixed magnitude, larger clusters are lower in surface brightness and thus more difficult to detect. However, even for objects with  $R_h = 0.25''$  (20 pc), the 50% completeness limit only rises to  $F814W=24.0$ , still well past the turnover of the GCLF.

Using these artificial globular tests as a guide, we then do the same automatic source detection procedure on the F475W image to select an initial sample of globular cluster candidates from the observed data. We detect all sources  $3\sigma$  above the background, and apply the same cuts on `semimajor_sigma` and area as described above. We also require sources to be detected in both the F475W and F814W imaging. Finally, we add a cut based on source ellipticity. Globular clusters are generally quite round; Galactic clusters all have major:minor

axis ratios of  $(b/a) > 0.75$  (Harris 1996), and the vast majority of M87 globular clusters have  $(b/a) > 0.7$  (Madrid et al. 2009)). Thus our final cut is to reject elongated sources with axis ratios  $(b/a) < 0.65$ . After these cuts, we are left with 298 compact sources detected in both images, likely consisting of a mix of foreground stars, compact background galaxies, and globular clusters — both those specifically associated with VCC 615, and perhaps others in the general Virgo intra-cluster population (e.g., Durrell et al. 2014; Longobardi et al. 2018).

With this initial sample of compact objects in hand, we refine the sample using a combination of F475W–F814W color and F814W aperture photometry. For each source, we measure aperture magnitudes in both F475W and F814W using apertures with 3 and 6 pixel radii, applying PSF aperture corrections (Bohlin 2016) to obtain total magnitudes and colors for the source. While these aperture magnitudes will underestimate the total magnitude of more extended sources like globular clusters, we use them here only for the initial photometric selection of cluster candidates; when characterizing the properties of the final cluster sample (Section 5) we use total magnitudes derived from `galfit` fitting of the sources. For the F814W data, we also calculate the difference between the 3- and 6-pixel aperture corrected magnitudes,  $\Delta_{(6-3)} \equiv m_6 - m_3$ . For unresolved point sources, these two magnitudes should be equivalent ( $\Delta_{(6-3)} \approx 0$ ), while for extended sources the additional light at larger radius will yield  $\Delta_{(6-3)} < 0$ . Injected clusters in our artificial globular cluster tests have  $\Delta_{(6-3)} \gtrsim -0.8$ , and our visual examination of real sources with  $\Delta_{(6-3)} \lesssim -0.8$  show most objects to be obviously extended background galaxies.

Using these metrics, we show in Figure 2 the properties of our initial sample of objects, where the left-hand panel shows the sources on a color-magnitude diagram (CMD), and the right hand panel shows  $\Delta_{(6-3)}$  vs F814W magnitude. In the CMD, the dashed horizontal line shows the expected peak magnitude of the VCC 615 GCLF, obtained by shifting the M87 GCLF peak (Peng et al. 2009) to the distance of VCC 615. Globular clusters are expected to span the color range  $1.0 < F475W-F814W < 2.0$  (see, e.g., Harris et al. 2020), shown in the highlighted region on the CMD. Within this color range we see a number of objects, clustered near the peak of the Virgo GCLF. Most of these objects have relatively blue colors ( $1.2 < F475W-F814W < 1.5$ ), consistent with the expectation for metal-poor globular clusters. At fainter magnitudes ( $F814W > 23.0$ , well below the GCLF turnover), the selection box becomes increasingly contaminated with background

galaxies, so we place a color-dependent lower limit on the magnitude selection; at a color of  $F475W-F814W=1.4$ , typical of metal-poor globular clusters, this lower limit is  $F814W=24.0$ , reaching about 90% of the way down the GCLF.

In the distribution of  $\Delta_{(6-3)}$  parameter, we see a tight clumping of objects at  $\Delta_{(6-3)} \approx 0$  which represent true point sources — foreground Milky Way stars, or other objects compact enough to be unresolved in our imaging. Below that sequence objects scatter to more negative  $\Delta_{(6-3)}$  values, indicative of more extended sources. The large number of sources at faint magnitudes ( $F814W > 23.0$ ) and  $\Delta_{(6-3)} < -0.25$  again shows the population of background sources, but many of the brighter sources have  $\Delta_{(6-3)} > -0.8$  where we expect globular clusters to lie. We thus construct a joint selection for cluster candidates with  $1.0 < F475W-F814W < 2.0$  and  $\Delta_{(6-3)} > -0.8$ . While this choice will include unresolved foreground stars in our sample, at this stage of the selection process we want to avoid excluding any very compact globular clusters with half light radii  $R_h \lesssim 1-2$  pc. In Figure 2, the 46 objects that pass both the color and compactness criteria are plotted as black stars if they are semi-resolved ( $-0.125 > \Delta_{(6-3)} > -0.8$ ), and red stars if they are star-like in compactness ( $\Delta_{(6-3)} > -0.125$ ).

Following the selection of globular cluster candidates based on color and  $\Delta_{(6-3)}$  compactness, we make one final visual check of the sources. Two of us (JCM and PRD) independently examined the deep F814W image and found 13 sources to be compact objects embedded in very diffuse and extended starlight, morphologically similar to the many background galaxies visible in the field. These types of objects were found largely at fainter magnitudes, where we expect background contamination to be high. Furthermore, of the nine objects bright enough to have deep *NGVS*  $u^*, g', i'$  photometry, all had colors inconsistent with those of globular clusters (see §4 below for more details). These 13 sources were thus removed from the candidate list, leaving us with a total of 33 star-like or slightly resolved globular cluster candidates to measure half-light radii for using `galfit`.

The selection of globular cluster candidates thus far has relied exclusively on the photometry and morphology of the sources in our *Hubble* imaging. However, for brighter sources we can also take advantage of additional ground-based photometry in other bandpasses. In particular, the deep *NGVS* imaging gives us  $u^*, g', i'$  photometry for sources brighter than  $F814W \approx 23.5$ , and the distribution of sources on the  $(u^* - g', g' - i')$  color plane has been shown to be an effective selection tool for globular clusters (Muñoz et al. 2014; Lim et al.

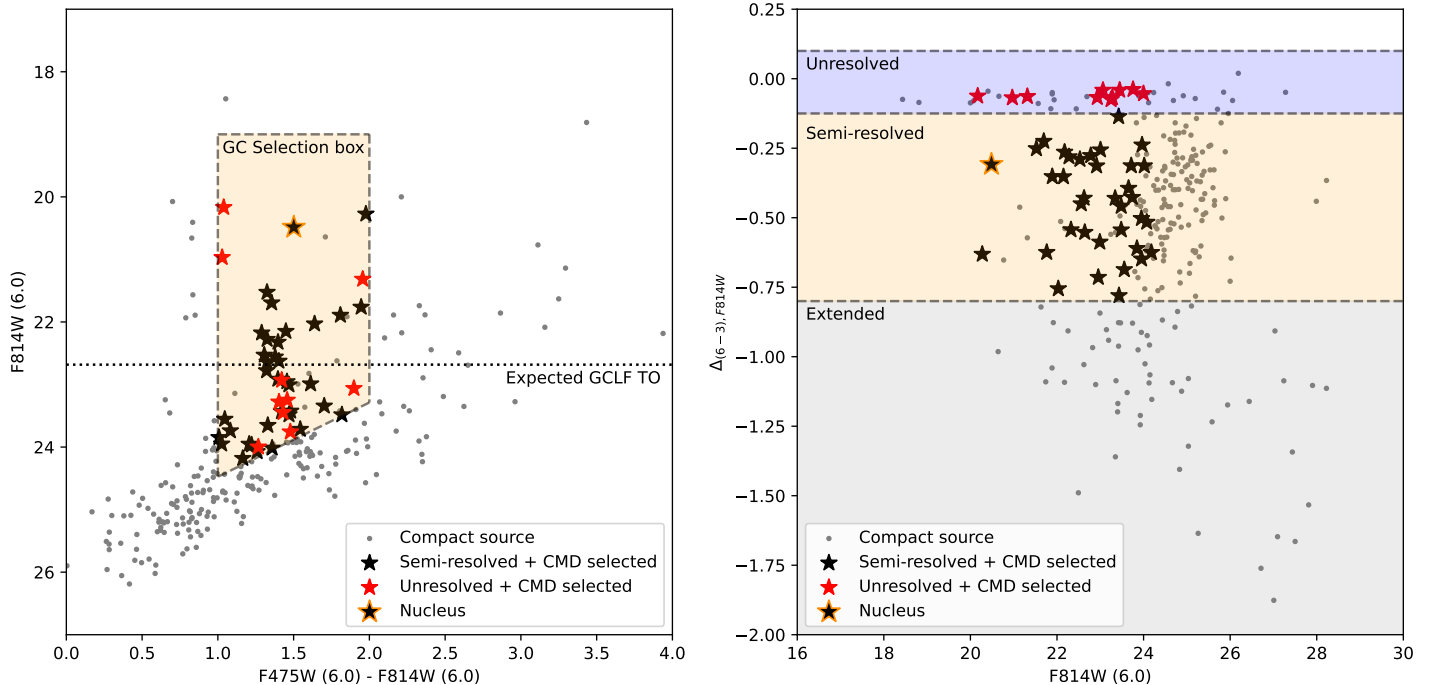


**Figure 2.** Photometric properties of compact sources. Left panel: F814W vs F475W–F814W color magnitude diagram, with the globular cluster selection box highlighted. Right panel:  $\Delta_{F814W (6-3)}$  vs F814W, with regions highlighted for unresolved objects, semi-resolved objects, and extended objects. Objects which are both color-selected and semi-resolved are shown as black stars; color-selected unresolved objects are shown as red stars. The nucleus of VCC 615 is highlighted in orange, and the dotted line on the CMD shows the M87 GCLF turnover magnitude (Peng et al. 2009), shifted to the VCC 615 distance of 17.7 Mpc.

2017). Figure 3 shows the distribution of our cluster candidates on the  $(u^* - g', g' - i')$  color plane, along with all (ground-based) point sources found within a  $5' \times 5'$  box around VCC 615 in the NGVS imaging. The dashed region shows the globular cluster selection box defined by Lim et al. (2017) based on the colors of the M87 globular cluster population. Eight objects lie outside the selection box, but one of them (at  $u^* - g', g' - i' \approx 1, 1$ ) has a background galaxy projected  $< 1''$  distant which likely contaminates the ground-based photometry. We retain that source in our candidate list but reject the other seven, leaving us with a total of 27 cluster candidates for further analysis.

#### 4. SIZES OF GLOBULAR CLUSTER CANDIDATES

To measure the half-light radii of our photometrically-selected globular cluster candidates, we use `galfit` to model each object using a Sérsic model convolved with the PSF derived from bright stars in the ACS field. We use Sérsic models rather than a King models because tests using `galfit` to fit artificial globular clusters (see below) showed Sérsic models to yield a higher frequency of successful fits than King models, while still accurately measuring the half-light radii of the clusters. We primarily rely on fitting the F814W imaging, due to its

deeper exposure time and higher signal to noise, but also fit the F475W imaging as a consistency check on the fitted models. For each source we make a  $250 \times 250$  pixel ( $12.5 \times 12.5$  arcsec) image cutout around the source, masking all objects  $3\sigma$  above the background (save for the source itself). We fit each source with free parameters being the half-light radius ( $R_h$ ), total F814W magnitude, Sérsic- $n$  parameter, and source ellipticity, as well as the locally estimated background flux level. As initial values, we input  $R_h = 1$  pixel,  $n = 4$ , a total magnitude equal to the 6-pixel aperture corrected magnitude, an ellipticity of  $b/a = 1$  and a sky level set by the overall median of the fully masked ACS field. The fitting process proved robust against reasonable variations of these input parameters.

To test the reliability of the `galfit` estimates of half-light radii and total magnitude, we used the artificial globular tests and processed all detected sources through `galfit` in the manner described above. We then compared the `galfit`-estimated properties of each source to its intrinsic (i.e., inserted) properties. For objects with half-light radii  $R_h > 0.025''$  (0.5 pixels), `galfit` reports a successful (i.e., converged) fit that only slightly overestimates (by about 5%) the intrinsic half-light ra-

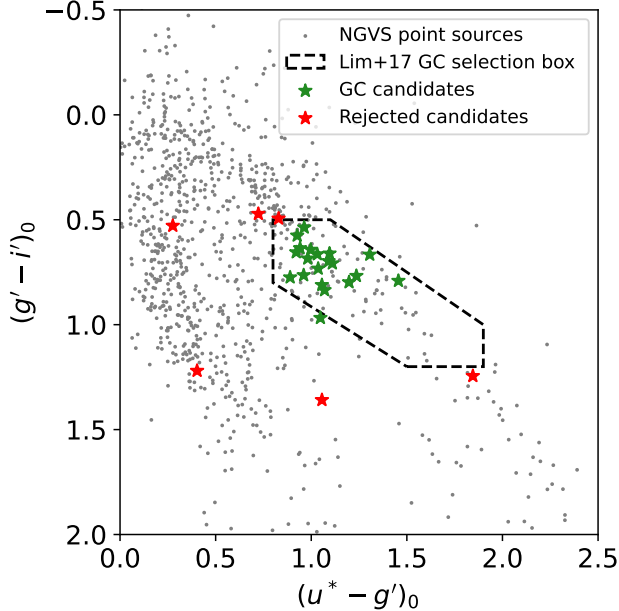


**Figure 3.** Ground-based NGVS  $u^*$ ,  $g'$ ,  $i'$  photometry of bright ( $F814W \lesssim 23.5$ ) compact sources in the VCC 615 field. Small gray dots show all ground-based point sources, and the dashed polygon is the  $u^*$ ,  $g'$ ,  $i'$  globular cluster selection criteria of Lim et al. (2017). Our *Hubble* globular cluster candidates that pass this selection are shown as green stars, while those that are rejected are shown as red stars.

dus. At slightly smaller radii ( $0.015'' < R_h < 0.025''$ , or  $0.3 < R_h < 0.5$  pix), `galfit` does not report successful convergence, but the fitted sizes remain accurate to  $\pm 20\%$ . When the intrinsic size is even smaller ( $R_h < 0.015''$ ), the `galfit` fits fail completely (unconverged fits with  $R_h \approx 0$ ), signifying an unresolved source. This  $0.015''$  limit on the measurable half-light radius corresponds to a physical size of 1.3 parsecs at the distance of VCC 615. The estimated total magnitudes are recovered to within typically  $\pm 0.025$  mag, except for objects with extremely small half-light radii ( $0.015'' < R_h < 0.025''$ ), where uncertainties in the fitted model lead to the estimated magnitudes being too bright by  $\approx 0.1$  mag.

The results of the `galfit` modeling of the photometric cluster candidates are shown in Figure 4. The left panel shows the fitted ellipticity as a function of F814W magnitude, where we only plot objects in which `galfit` reports a successful (i.e., resolved) fit. The candidates populate two distinct regions: the majority have axis ratios  $b/a \approx 0.8-0.95$ , while a handful show axis ratios  $b/a \lesssim 0.65$ . We use this ellipticity as an additional selection criterion. Milky Way globular clusters all have  $b/a > 0.75$  (Harris 1996), and Madrid et al. (2009) show

that the ellipticity distribution of M87 globular clusters, measured in a very similar manner to what is done here, show a peak at  $b/a = 0.9$ , with very few flattened clusters at  $b/a < 0.6$ . Interestingly, however, the brightest of these flattened sources in our sample has been confirmed spectroscopically by Toloba et al. (2023) to have a Virgo-like velocity of  $2090 \text{ km s}^{-1}$ . We keep this object but reject the other three, leaving us with 24 globular cluster candidates in our sample.

The right two panels in Figure 4 show the fitted half-light radius of each candidate as a function of photometric compactness ( $\Delta_{(6-3)}$ ) and F814W magnitude. In these panels, we plot the `galfit`-reported size even for objects where the fit failed and the objects are considered unresolved (the gray shaded area in the right two panels). Two objects fall just below this cutoff at  $R_h = 0.015''$  (1.2 pc); while we classify these objects as unresolved, in our artificial globular tests a small fraction of objects with sizes below that limit yielded accurate but unconverged fits, and an examination of the model residuals for these two sources show a clean subtraction. Thus these objects may be just barely resolved, but for consistency in building the final sample we place them in the unresolved category.

The other object which does not have a converged fit is the nucleus, which lies above the otherwise regular sequence of objects where the fitted size decreases smoothly with the  $\Delta_{(6-3)}$  compactness parameter. The structure of the nucleus is rather complex (see the more complete discussion in Section 6, following), and at the depth of the F814W image we start to resolve individual bright stars in the outskirts, all of which likely complicate the optimization of the fit parameters. However, the fit residual again shows reasonably clean model subtraction, and the fits in F814W and F475W — while both unconverged — show good agreement.

We ran two additional tests to assess the robustness of the size estimates for the globular cluster candidates. We ran `galfit` on both the F475W and F814W images, and also independently measured sizes of the artificial globular clusters on the F814W image using the source fitting algorithm ISHAPE (Larsen 1999). The lower signal-to-noise in the F475W image leads to larger uncertainties (and more unconverged fits) than in the F814W imaging, but both `galfit` measures follow the 1:1 line with a scatter of only 0.08 dex for objects with good fits. Comparing the  $R_h$  `galfit` F814W results to those derived from ISHAPE, we see an even tighter relationship with scatter of only 0.05 dex around the one to one line for well-fit objects, albeit with increased scatter for the largest objects. Interestingly, for the two barely-resolved objects the unconverged the

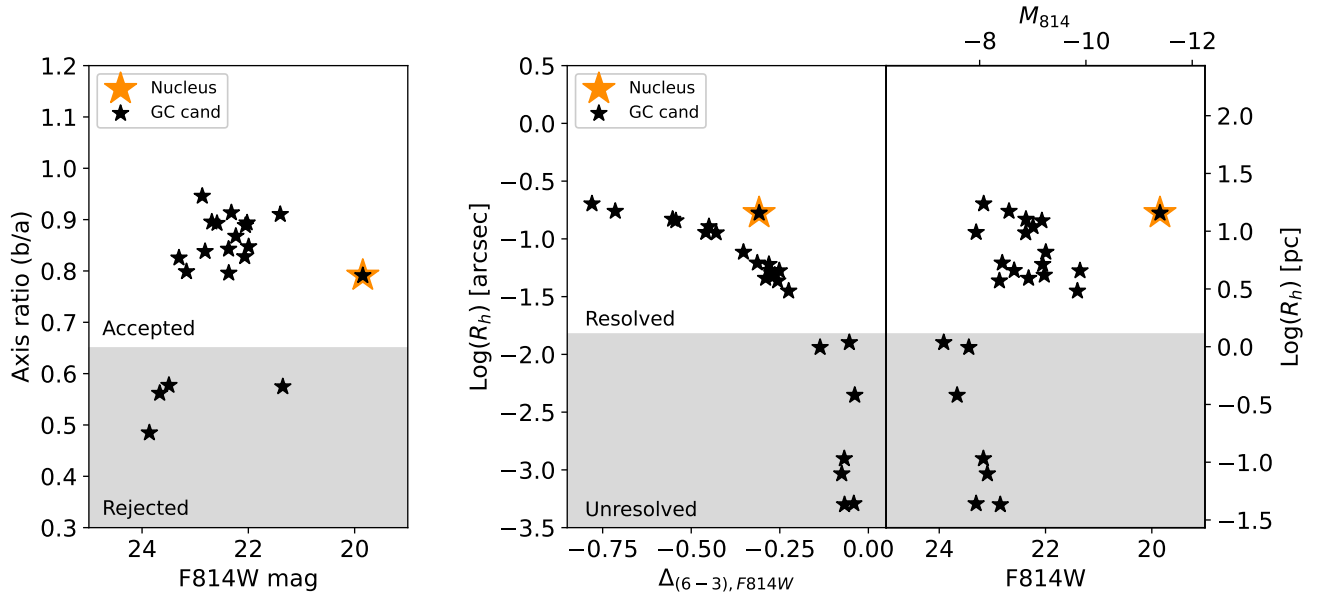


**Figure 4.** Results of `galfit` modeling of photometric globular cluster candidates. Left panel: Ellipticity vs F814W magnitude. The grey shaded area shows the rejection criteria of  $(b/a) < 0.65$ , although the brightest object in the rejection region has spectroscopic confirmation from Toloba et al. (2023) and is kept in the sample. Right panels: Half-light radius vs  $\Delta_{(6-3)}$  and F814W magnitude for objects which pass the  $(b/a) < 0.7$  criterion. In these panels, we plot all the `galfit`-reported half-light radii, but for objects smaller than  $R_h = 0.015''$  (grey shaded region), these fits are not meaningful and the objects are considered unresolved. In each panel, the nucleus is highlighted as a large gold star.

`galfit` and ISHAPE results both show  $R_h \approx 0.25$  pixels ( $0.01''$ ), again suggesting these objects may be correctly measured. We also note that while the `galfit` models did not fully converge while fitting the nucleus, the `galfit` F475W and F814W fits agree and give a clean model subtraction despite reporting unconverged fits. Attempts to fit the nucleus using ISHAPE were unsuccessful.

Armed with size measurements for our globular cluster candidates, we plot in Figure 5 the CMD and sky positions of all the objects, sorted by classification. The resolved sources (with sizes  $R_h = 0.015\text{--}0.2''$ , or  $1.3\text{--}17$  pc) cluster tightly both on the CMD and in the inner  $1.5R_{e,*}$  of the galaxy. The mean color of these objects (excluding the nucleus) is  $F475W - F814W = 1.38$  with a scatter of  $\sigma = 0.06$  mags. The nucleus itself stands out in the CMD as being much brighter than the other resolved sources, with a somewhat redder color of  $F475W - F814W = 1.50$ . Of the two faintest resolved sources, which start to overlap with the sea of background sources at  $F814W \approx 23.5$ , one is located within  $1.5R_{e,*}$  and the other (at the top edge of the ACS field) is found at  $3R_{e,*}$ . Both these objects are kept in the globular cluster sample.

The unresolved sources do not cluster as strongly around the galaxy spatially, but are mostly found in the same region of the CMD as the resolved sources. Two of the unresolved sources are found at the faintest extreme

of the CMD selection region, and may be background sources. One of these is distinct in color from the bulk of the resolved sources, and is also located just outside the red circle at  $r = 120''$ . This object is particularly likely to be a contaminant and is removed from our globular cluster sample. The other object has a similar color to the resolved candidates, was one of the two “just unresolved” objects seen in Figure 4, and is located inside the  $r = 120''$  circle, at  $r \approx 3R_{e,*}$  (the right edge of the ACS field). The other “just unresolved” object is found inside  $1.5R_{e,*}$  at the bottom right. Both these sources, along with the other four unresolved objects at similar colors in the CMD, are all kept in our sample of likely globular clusters.

Finally, if we look at the spatial distribution of rejected sources (visually identified galaxies and compact sources rejected based on their flattening or  $u^*g'i'$  colors), none of those sources cluster around VCC 615, nor are they similar in their CMD properties to the resolved and unresolved sources. The flattened sources are all found at the bottom edge of the CMD selection box, overlapping with background sources, while the  $u^*g'i'$ -rejected sources fall mostly at the extreme edges of the color selection range. Thus we feel confident that our source rejection criteria are not rejecting bona-fide globular cluster candidates.

All told, we have a total of 23 objects (17 resolved, 6 unresolved) in our globular cluster sample. We give



the detailed properties of all objects in our final globular cluster sample in Table 3. We also cross-match the sample against the spectroscopic sample of Toloba et al. (2023), who targeted bright ( $F814W \lesssim 23$ ) globular clusters around VCC 615 from the Lim et al. (2020) sample to derive the galaxy’s dynamical mass. Nine sources (including the nucleus) are in both our catalog and the Toloba et al. (2023) spectroscopic catalog. All nine of those sources lie within  $\pm 125 \text{ km s}^{-1}$  of the VCC 615 systemic velocity ( $2089 \text{ km s}^{-1}$ , Toloba et al. 2023), placing them not only within the Virgo Cluster, but also almost certainly associating them with VCC 615 itself. The VCC-like velocities of the spectroscopically confirmed objects suggests that we have little-to-no contamination from intracluster globular clusters in our sample.

Finally, we can compare our sample of VCC 615 globular clusters to the ground-based sample of Lim et al. (2020), which uses imaging from the *Next Generation Virgo Survey* (Ferrarese et al. 2012) to photometrically select 23 globular cluster candidates within a  $120''$  radius of VCC 615. Of those 23 sources, three are outside our ACS FOV, two are resolved as background galaxies, and two are rejected by the  $u^*$ ,  $g'$ ,  $i'$  selection criteria. The latter two sources are almost certainly foreground stars: not only are they  $u^*$ ,  $g'$ ,  $i'$ -rejected, they also lie at the extreme color boundaries of the CMD selection region shown in Figure 2 and are unresolved in our *galfit* size estimates. The remaining 16 sources from the Lim cataloged are confirmed in our catalog as well, including all 12 candidates inside  $1.5R_e$ . Our catalog also contains an additional 7 relatively faint cluster candidates ( $F814W > 23.2$ ) in addition to those in common with the Lim et al. (2020) sample.

## 5. PROPERTIES OF THE VCC 615 GLOBULAR CLUSTER SYSTEM

Here we compare the properties of the VCC 615 globular cluster system to those in galaxies more generally. Studies of globular clusters in other UDGs have hinted at differences between their globular cluster systems and those in more ‘normal’ high surface brightness, but such studies are often plagued by significant uncertainties, due both to the relatively small number of globular clusters (and associated high contamination fractions) and distance uncertainties to the host galaxies. In the case of VCC 615, our *Hubble* data has provided for a very clean selection of globular clusters, with a very low contamination fraction. Furthermore, the galaxy has a well-determined TRGB distance of  $d = 17.7^{+0.6}_{-0.4} \text{ Mpc}$  (Mihos et al. 2022), significantly reducing the uncertainties

on distance-dependent quantities such as luminosity and physical size.

In our discussion, we focus first on the intrinsic properties of the VCC 615 globular clusters themselves, then turn to the connection between the host galaxy and the globular cluster system as a whole. Because the nucleus is so distinct photometrically and structurally from the other cluster candidates (see Section 6, following), in general we remove it from the sample when discussing the properties of the VCC 615 globular clusters.

### 5.1. Properties of the individual globular cluster candidates

#### 5.1.1. Luminosity Function

We first examine the luminosity function of the globular cluster candidates, shown in Figure 7. Here we break out the sample in two ways: first by showing all candidates in the ACS field, and also by showing the subsample of candidates found within  $R = 1.5R_{e,*}$  of the photometric center of VCC 615. While the full sample is larger in number ( $N_{GC} = 22$ , not including the nucleus), it is also more likely to contain a handful of contaminants, predominantly at fainter magnitudes. Conversely, the inner sample of candidates within  $1.5R_{e,*}$  is smaller ( $N_{GC} = 14$ ), but likely has fewer contaminants. When constructing the luminosity function, we use the *galfit* F814W magnitudes for resolved sources successfully fit by *galfit*, while for unresolved objects we use the aperture-corrected six-pixel aperture magnitudes from *photutils*.

To characterize the luminosity function, we use the Bayesian fitting package *emcee* (Foreman-Mackey et al. 2019) to model a Gaussian luminosity function for each sample with turnover magnitude  $\mu_0$  and width  $\sigma$  for the two samples, factoring in the magnitude limit of  $F814W_{\text{lim,GC}} = 24.0$  set by our selection box in the CMD in Figure 5. Excluding the nucleus from the fit, we obtain  $\mu_0 = 22.78^{+0.39}_{-0.22}$ ,  $\sigma = 0.86^{+0.36}_{-0.19}$  for the full sample, and  $\mu_0 = 22.55^{+0.39}_{-0.24}$ ,  $\sigma = 0.84^{+0.47}_{-0.21}$  for the subsample within  $R = 1.5R_{e,*}$  (see Table 2). The difference between the fitted turnover magnitude between the two samples is within the overall uncertainty of the fit, and adding the nucleus to the samples does not change the turnover magnitude in any significant way.

While including the nucleus in the GCLF fit does not change the fitted turnover magnitude, it does significantly broaden the fitted dispersion, to values of  $\sigma = 1.34 - 1.40$ . A GCLF this broad is uncharacteristic of a low luminosity system like VCC 615. Studies show that the GCLF width is a declining function of host galaxy luminosity (e.g., Durrell et al. 1996; Jordán et al. 2006; Miller & Lotz 2007; Villegas et al. 2010).

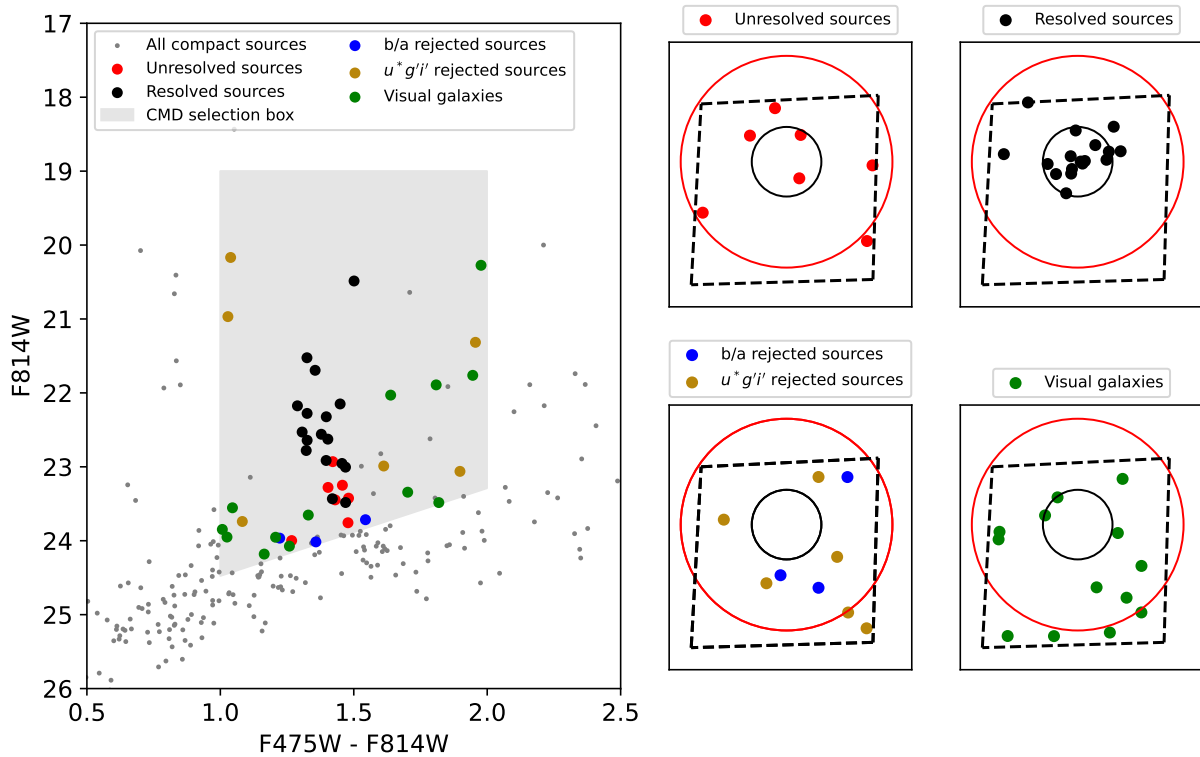


**Figure 5.** Photometric and spatial plots of compact sources in the ACS field. Small grey dots show all compact sources. Larger dots show sources selected jointly on their location in the CMD and on their  $\Delta_{(6-3)}$  compactness factor, color coded by classification. Unresolved sources (red) have  $R_h < 0.015''$  (1.3 pc), while resolved sources (black) have measured half-light radii in the range  $R_h = 0.015'' - 0.2''$  (1.3–17 pc). Objects rejected by their flattened axis ratio  $b/a < 0.65$  are shown in blue, objects rejected by their  $u^*g'i'$  colors are shown in magenta, and objects visually classified as galaxies are shown in green. The inner black circle has a radius of  $1.5R_{e,*}$  while the outer red circle has a radius of  $120''$  ( $\approx 5R_{e,*}$ ). The field of view of our ACS imaging is shown by the dashed black box.

Dispersions as large as that seen in our fits that include the VCC 615 nucleus are more typical of massive ellipticals such as M87 (Peng et al. 2009) and M49 (Jordán et al. 2007) in Virgo, while the lower dispersion for fits without the nucleus are much more characteristic of low luminosity systems (Lotz et al. 2004; Jordán et al. 2006; Villegas et al. 2010). For this reason, as well as the large gap between the brightness of the nucleus and the next brightest object in the sample, we adopt the fitted values for  $\mu_0$  and  $\sigma$  from the (nucleus-free) full sample as most reflective of the overall GCLF in VCC 615. Integrating this fitted GCLF over all magnitudes, we find that our cluster sample is close to fully complete: only  $\approx 8\%$  of the total GCLF lies below our  $F814W_{\text{lim,GC}} = 24.0$  magnitude limit.

Studies of globular cluster systems in UDGs have revealed that at least some systems have populations of overly luminous globular clusters, skewing the peak of the GCLF to brighter magnitudes and complicating the

use of the GCLF as a distance indicator for these systems. For the VCC 615 GCLF at a 17.7 Mpc distance, the peak magnitude lies at  $M_{F814W} = -8.45$  for the full sample, and is slightly brighter ( $M_{F814W} = -8.68$ ) for the inner sample. While this is comparable to the GCLF peak magnitude for luminous early-type galaxies ( $M_{F814W} \approx -8.5$ , e.g., Kundu & Whitmore 2001; Peng et al. 2009), studies show that the peak magnitude is fainter for low luminosity galaxies. For example, Miller & Lotz (2007) show that the GCLF in Virgo dEs peaks at  $M_I = -8.25$  (adjusted for a Virgo distance of 16.5 Mpc), while the relationship between GCLF peak magnitude and galaxy luminosity derived by Villegas et al. (2010) argues that the VCC 615 GCLF peak should be  $\approx 0.3$  mag fainter than in bright ellipticals. Thus our derived GCLF peak in VCC 615 appears slightly brighter than expected for a galaxy of its luminosity, by about 0.3–0.5 magnitudes depending on the cluster sample used (full vs. inner). However, this is close to

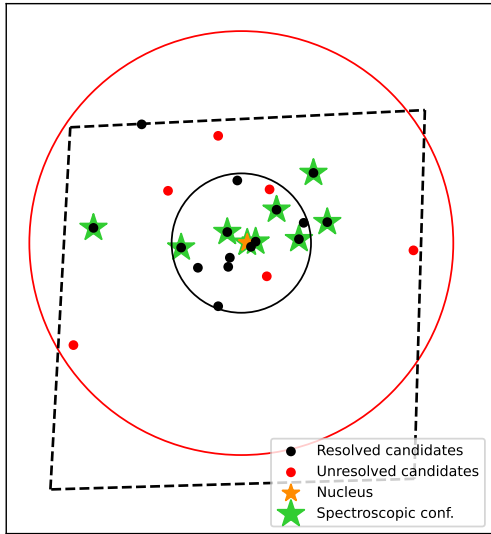


**Figure 6.** Spatial distribution of our globular cluster candidates in VCC 615. Black symbols are the semi-resolved candidates, red symbols are the unresolved candidates. The nucleus is shown with a gold star, while spectroscopically confirmed sources (Toloba et al. 2023) are shown with a green star. The black circle has a radius of  $1.5R_{e,*}$ , the red circle has a radius of  $120''$  ( $\approx 5R_{e,*}$ ), and the dotted lines show the ACS field of view.

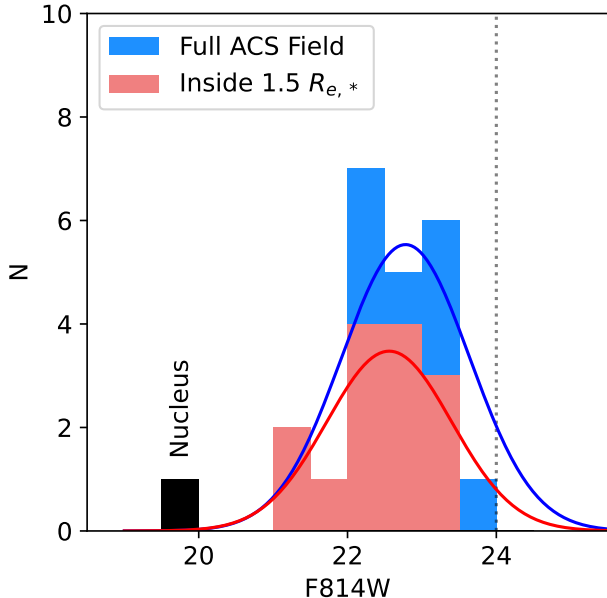


**Figure 7.** Luminosity function for the globular cluster candidates in VCC 615, for both the full sample and for objects only within  $1.5R_{e,*}$ . The grey dotted line shows the limiting magnitude of the sample,  $F814W_{\text{lim}} = 24.0$ . The blue and red lines show the Gaussian fit to the full and inner samples, respectively, with the nucleus omitted from the fits.

**Table 2.** Gaussian GCLF Fits

|             |          | All globular clusters   | Inside $1.5R_{e,*}$     |
|-------------|----------|-------------------------|-------------------------|
| w/ nucleus  | $\mu_0$  | $22.93^{+0.56}_{-0.40}$ | $22.54^{+0.61}_{-0.45}$ |
|             | $\sigma$ | $1.34^{+0.39}_{-0.34}$  | $1.40^{+0.39}_{-0.40}$  |
| w/o nucleus | $\mu_0$  | $22.78^{+0.39}_{-0.22}$ | $22.56^{+0.40}_{-0.25}$ |
|             | $\sigma$ | $0.86^{+0.37}_{-0.19}$  | $0.84^{+0.48}_{-0.22}$  |

the  $\sim 0.3$  mag uncertainty in the measurement, and we see no evidence for a large population of extremely luminous clusters (overluminous by 1.5-2 mags) such as those found in the UDGs NGC 1052-DF2 and -DF4, (van Dokkum et al. 2018a; Shen et al. 2021a,b).

### 5.1.2. Colors

Globular cluster colors provide insights into both the characteristic metallicity and metallicity spread of the cluster population. The color distribution of the globular clusters in VCC 615 is fairly tight (see Figure 5) and unimodal, with no evidence of the separate blue and red populations seen around more massive galaxies (e.g., Kundu & Whitmore 2001; Peng et al. 2006; Harris et al. 2006; Lee et al. 2008; Harris 2023). Calculating the colors from the six-pixel aperture magnitudes, for the full cluster sample we find a mean color of  $F475W-F814W=1.40$ , with dispersion of only  $\sigma = 0.06$  magnitudes, and these values are unchanged if we consider only the objects in the inner  $1.5R_{e,*}$  of the galaxy.

This color is comparable to the blue (more metal-poor) globular cluster populations seen around much larger galaxies (e.g., Peng et al. 2006; Cho et al. 2016; Harris et al. 2017, 2020; Harris 2023), and are also consistent with globular clusters observed in those UDGs with large enough (typically  $N_{GC} > 10$ ) populations for such measurements. Using the most recent ACS zero-points, our color translates to  $(F475W-F814W)_{AB} = 0.88$ . This value is consistent with the mean colors of globular clusters in Coma cluster UDGs measured by Amorisco et al. (2018) and Saifollahi et al. (2022) ( $(F475W-F814W)_{AB} = 0.91$  and  $0.95$ , respectively), as well as the  $(g-I)_{AB} = 0.91 \pm 0.05$  color for clusters in the Coma UDG DF17 (Beasley & Trujillo 2016). These colors are, in turn, similar to that of the blue globular clusters observed in Coma's intracluster environment ( $(g-I) = 0.89$ ; Peng et al. 2011). While our colors are indicative of a metal-poor population, the values above tend to be slightly redder (more metal-rich; assuming comparable ages) than that of dwarf galaxies of similar luminosity. Using the relations presented by

Harris (2023) our mean color translates to a metallicity  $[Fe/H] \sim -1.2$  (assuming an age of 12 Gyr), which is a value expected for somewhat higher luminosity systems than VCC 615. This may be indicative of the higher total masses observed in UDGs with significant globular cluster populations; our mean metallicity is broadly consistent with, albeit at the high end, of galaxies with total masses  $\sim 10^{10-11} M_{\odot}$ . This tendency for (at least some) massive UDGs to have cluster metallicities higher than expected for dwarf galaxies of similar  $M_V$  has also been seen by Beasley & Trujillo (2016) and Janssens et al. (2022).

While the color dispersion ( $\sigma = 0.06$ ) in our globular cluster candidates is small it is not as extremely monochromatic as found in some other UDGs (Müller et al. 2021; van Dokkum et al. 2022; Janssens et al. 2022; Fielder et al. 2023), and there are examples of larger color dispersions in more luminous UDGs (Lim et al. 2020; Saifollahi et al. 2022). We see no sign of clusters redder than  $F475W - F814W = 1.5$ , where more metal-rich clusters would reside (Harris 2023). While a large population of metal-rich clusters is unlikely in a low luminosity galaxy like VCC 615 (e.g., Lotz et al. 2004; Peng et al. 2006) this also argues that we have no contamination from metal-rich intracluster globular clusters in the surrounding Virgo environment (e.g., Durrell et al. 2014; Longobardi et al. 2018).

### 5.1.3. Sizes

While the luminosity function of the VCC 615 globular clusters appear normal for a galaxy of its luminosity, we do see an excess of overly large clusters in the sample. Figure 8 shows the half-light radii of the globular cluster candidates in VCC 615, as a function of both galactocentric distance and F814W magnitude. The sizes show a significant spread, from unresolved sources with  $R_h < 1.5$  pc, to larger objects up to  $R_h \approx 17$  pc. Some of these objects could in principle be contaminants, but three of them are spectroscopically confirmed to have Virgo-like velocities within  $125 \text{ km s}^{-1}$  of VCC 615 (Toloba et al. 2023). Furthermore, two other large  $R_h$  objects that lack spectroscopic confirmation are located in the inner  $10''$  ( $0.4 R_{e,*}$ ) of the galaxy, where contamination is statistically less likely. Thus it appears probable that many (if not all) of these objects are large star clusters physically associated with VCC 615.

At first glance the sizes of these large clusters may seem at odds with those of more typical globular clusters observed in other (larger) galaxies, where the median half-light radius is  $R_h \approx 2.5 - 3.5$  pc (e.g., Larsen et al. 2001; Jordán et al. 2009; Harris 2009; Madrid et al. 2009; Puzia et al. 2014). However, populations of such large

“extended star clusters” (ESCs) with sizes  $R_h > 7$  pc have been found in the outer halos of the Milky Way, M31, and several other nearby galaxies (Mackey & van den Bergh 2005; Huxor et al. 2005, 2014; Puzia et al. 2014; Mackey et al. 2019). These ESCs are similar in size and luminosity ( $M_V > -8$ ) to the populations of “faint fuzzies” or “diffuse star clusters” found in other large galaxies as well (Larsen & Brodie 2000; Chandar et al. 2004; Peng et al. 2006; Forbes et al. 2013; Liu et al. 2016), although those objects tend to be redder or more metal-rich than the ESCs observed in the Milky Way or M31. Note here that we distinguish ESCs from objects like ultra-compact dwarf galaxies (UCDs) and the nuclei of dwarf galaxies, which are similar in sizes but typically much more luminous. For example, as shown in Figure 8, while the nucleus of VCC 615 has comparable size to some of the ESCs we find the galaxy, it is  $\approx 2.5$  magnitudes brighter than the rest of the ESC population.

In our sample of VCC 615 globular cluster candidates, the fraction of objects with large half-light radii ( $R_h > 9$  pc) is relatively high: 7/22, or 32%. This is larger than the fraction of similarly large clusters found in the Milky Way (30/167 or 18%, based on the catalog of Baumgardt et al. 2023), although the fraction of large clusters increases in the Milky Way’s outer halo (e.g., Mackey & van den Bergh 2005). A similar trend is seen in M31, where  $\sim 40\%$  of the clusters at large projected galactocentric radii ( $R_{GC} > 25$  kpc) have  $R_h > 9$  pc (Mackey et al. 2019). Dwarf galaxies also have significant populations of ESCs of similar size to those we see in VCC 615 (e.g., Jordán et al. 2005; Sharina et al. 2005; Georgiev et al. 2009; Da Costa et al. 2009; Hwang et al. 2011; Cole et al. 2017); for example, roughly half the old globular clusters discovered in the M81 group dIrr galaxy IC 2574 have  $R_h > 7$  pc (Karim et al. 2024). Thus the relatively high fraction of large clusters we find in VCC 615 is similar to that found in dwarf galaxies and the outskirts of larger galaxies, consistent with the idea that the weaker tidal fields found in low density environments are particularly beneficial for the survival of such extended globular clusters (Mackey & van den Bergh 2005; Hurley & Mackey 2010; Hwang et al. 2011; Mackey et al. 2019).

Thus the size distribution of globular clusters in UDGs more generally may also hold information regarding their total mass or, more specifically, tidal fields. While there are only a few UDGs with measured globular cluster sizes, there are at least some indications that they too host significant populations of extended clusters. Studies of the UDG NGC1052-DF2 have shown that many of its bright, spectroscopically-confirmed clusters have large half-light radii (van Dokkum et al. 2018b; Tru-

jillo et al. 2019; Ma et al. 2020), although these clusters are also more luminous than the ESCs we find in VCC 615. Müller et al. (2021) also find a wide range in  $R_h$  for the globular clusters in the UDG MATLAS-2019. While the brighter, spectroscopically-confirmed clusters in that galaxy were all reasonably compact ( $R_h < 7\text{pc}$ ), many fainter candidates were detected with larger half-light radii, although without spectroscopic confirmation some of those objects may be background contaminants. Further studies of globular cluster sizes in UDGs will thus be extremely important in probing the connection between cluster properties and their host galaxies, and constraining the dark matter halos of UDGs.

5.2. Properties of the globular cluster system

Turning to the properties of the VCC 615 globular cluster system as a whole, of particular interest is the total number of globular clusters  $N_{GC}$ . Based purely on our observed counts (again, not including the nucleus), we have 22 globular cluster candidates, including both resolved and unresolved objects. However, at the faint end of the distribution, we become susceptible to background contamination; given the increasing density of background sources in the bottom  $\sim 0.75$  mag of the CMD selection box, we might expect that 2–4 of the faintest candidates may be contaminants. At the same time, our areal coverage is only complete out to  $75''$  ( $3R_{e,*}$ ), and we may be missing a handful of globular clusters that lie outside the ACS field of view (and indeed, the ground-based study of Lim et al. 2020 identified three cluster candidates that lie just off our ACS field.) Thus, purely from the raw counts, an observed cluster population of  $N_{GC,obs} = 22 \pm 3$  seems reasonable.

We address this question more quantitatively by adopting a model for the spatial distribution of the globular cluster system. If we use the Bayesian fitting package `emcee` to fit a Sérsic model to the data, including a flat distribution for contaminants:

$$\Sigma(R) = \Sigma_e \exp\left\{-b_n \left[\left(\frac{R}{R_e}\right)^{1/n} - 1\right]\right\} + \Sigma_b$$

we derive  $n = 1.94^{+0.76}_{-0.66}$ ,  $R_e = 38.8^{+15.2}_{-9.7}$  arcsec,  $\log(\Sigma_e) = -2.3^{+0.74}_{-0.40}$ ,  $\log(\Sigma_b) = -4.0^{+0.31}_{-0.53}$ . The fitted value for Sérsic- $n$  is consistent with the results for globular cluster systems more generally, which span the range  $1 \lesssim n \lesssim 4$  with a median value of  $n \approx 2$  (Lim et al. 2024). These fits also provide a total integrated globular cluster count, including sources outside the ACS field of view, of  $N_{GC,tot} = 23.1^{+6.0}_{-5.0}$  and set the number of contaminants on the FOV at  $N_{cont} = 3.7^{+3.9}_{-2.6}$ . These numbers compare well to the estimates based on the raw counts given above. Finally, we make one final and small correction for photometric incompleteness.

As shown in the discussion of the GCLF above we have a completeness fraction of  $\approx 0.92$ , and factoring this in yields our final estimate of the total globular cluster population:  $N_{GC,tot} = 25.1^{+6.5}_{-5.4}$ . This estimate is slightly smaller than the Lim et al. (2020) estimate of  $N_{GC,tot} = 30.3 \pm 9.6$  based on ground-based imaging, but consistent within the uncertainties.

Previous studies have shown that the globular cluster populations around UDGs can be quite diverse, likely reflecting the variety of formation channels that lead to the formation of a UDG. A number of UDGs host anomalously large numbers of globular clusters for their total luminosity (e.g., Lim et al. 2018, 2020; Müller et al. 2021; Danieli et al. 2022; Fielder et al. 2023; Marleau et al. 2024), with specific frequencies as high as  $S_N \sim 100 - 200$ . In Virgo, the globular cluster specific frequency in UDGs is higher than that of the classical Virgo dwarf population (Lim et al. 2020), and both UDGs and normal dwarfs show increasing  $S_N$  values at lower luminosities (Miller & Lotz 2007; Lim et al. 2020). Coupling our VCC 615 globular cluster count with the total V-band luminosity of the galaxy ( $M_V = -14.1$ , Lim et al. 2020, adjusted for a 17.7 Mpc distance) we derive a globular cluster specific frequency of  $S_N = 55.5^{+14.5}_{-12.0}$ , significantly higher than normal Virgo dwarfs, and even higher than the average for Virgo UDGs of similar luminosity (Lim et al. 2020). Following the correlation between globular cluster counts and total dynamical mass in galaxies (e.g., Blakeslee 1997; Peng et al. 2008; Harris et al. 2013; Hudson et al. 2014; Harris et al. 2017), such a high specific frequency for VCC 615 argues for a large mass-to-light ratio for the galaxy, consistent with that inferred for the galaxy from the kinematics of its bright globular clusters (Toloba et al. 2018, 2023).

Indeed we can use VCC 615’s total globular cluster count to provide an independent estimate of the galaxy’s total mass. Using the  $N_{GC}-M_{tot}$  relationship from Harris et al. (2017), VCC 615’s total globular cluster population of  $N_{GC,tot} = 25.1$  yields a total mass of  $M_{tot} = 1.6 \times 10^{11} M_\odot$ . Alternatively, adopting a globular cluster mean mass of  $10^5 M_\odot$  (Harris et al. 2017) and using the Harris et al. (2017) relationship between total galaxy mass and total cluster mass, we derive a total mass of  $M_{tot} = 8.7 \times 10^{10} M_\odot$ . Given the galaxy’s stellar mass of  $M_* = 7.3 \pm 1.1 \times 10^7 M_\odot$  (Roediger et al. in prep), these values indicate a stellar mass – halo mass ratio of  $\log(M_*/M_h) \approx -3.1 \pm 0.3$ , where the uncertainty comes largely from the scatter in the globular cluster scaling relationships (Harris et al. 2017). Models of the stellar mass – halo mass relationship (e.g., Behroozi et al. 2010, 2013; Moster et al. 2013) argue for higher values ( $\log(M_*/M_h) \approx -2.0$  to  $-2.5$ )

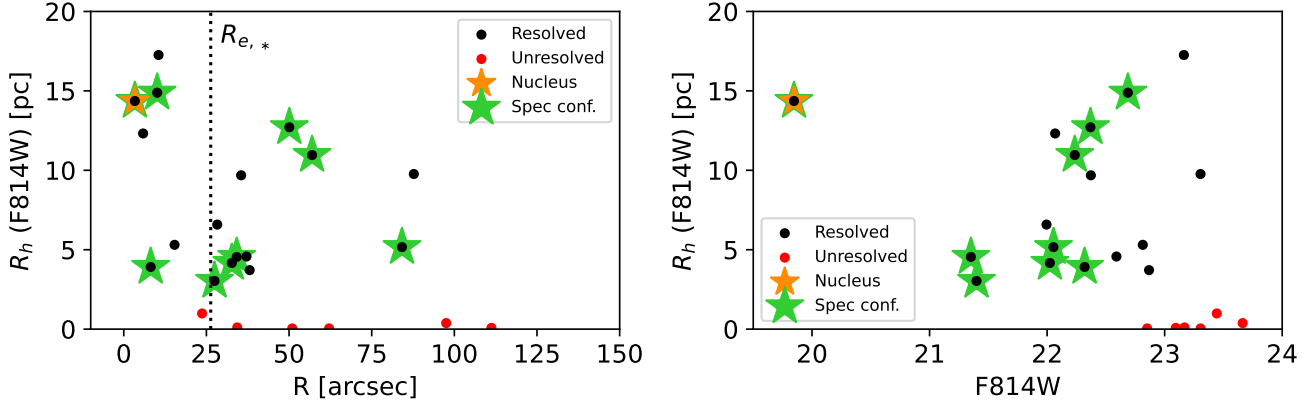


**Figure 8.** *galfit*-measured half-light radii ( $R_h$ ) for the globular cluster candidates in VCC 615. Left panel:  $R_h$  vs galactocentric radius. Right panel:  $R_h$  vs F814W magnitude. Black and red points show resolved and unresolved sources, respectively, and spectroscopically confirmed VCC 615 clusters are highlighted with green stars. The nucleus is highlighted in gold as well.

for galaxies of comparable mass to VCC 615. Alternatively, we can adopt a halo mass profile to calculate the inferred mass-to-light ratio inside the effective radius of the globular cluster system ( $R_{e,GC}$ ) and compare it to that measured kinematically by Toloba et al. (2023) ( $M_{1/2}/L_{1/2,V} = 148_{-144}^{+181} M_{\odot}/L_{\odot}$ ). Adopting an NFW halo profile (Navarro et al. 1997) and a halo concentration  $c = 8$  characteristic for halos of this mass (Dutton & Macciò 2014) we can scale our total mass to the mass inside the effective radius. If we use the same  $R_{e,GC} = 23.3''$  value used by Toloba et al. (2023), we derive large mass-to-light ratios of  $M_{1/2}/L_{1/2,V} \approx 99 M_{\odot}/L_{\odot}$  and  $79 M_{\odot}/L_{\odot}$  for our halo masses derived from the  $N_{GC}-M_{tot}$  and  $M_{GC}-M_{tot}$  relations, respectively. If we use the larger value of  $R_{e,GC} = 38.3''$  derived from our sample above, these values rise to  $M_{1/2}/L_{1/2,V} \approx 135 M_{\odot}/L_{\odot}$  and  $116 M_{\odot}/L_{\odot}$ , respectively. Thus the total mass and high mass-to-light ratio for VCC 615 inferred from the globular cluster counts is consistent with the galaxy having an overly massive dark halo, as argued by Toloba et al. (2023).

The fitted size of the VCC 615 globular cluster system ( $R_{e,GC} = 38.8_{-9.7}^{+15.2}$  arcsec, or  $3.3_{-0.8}^{+1.3}$  kpc) can also provide insight into the origin of the system. Recent work by Lim et al. (2024) derives scaling relationships between the size of globular cluster systems and the stellar half-light radius and stellar mass of their host galaxies. In this work, Lim et al. (2024) shows that these scaling relationships behave differently for the red and blue globular cluster sub-systems in galaxies, which are thought to trace clusters formed *in-situ* versus ones later accreted, respectively. At fixed stellar half-light radius, the size of the VCC 615 globular cluster system is much smaller than expected for blue (accreted) clusters and more typical of the red (*in-situ*) systems, suggest-

ing that the globular cluster system in VCC 615 was formed along with the galaxy itself. However, the tightest correlation found by Lim et al. (2024) is between the size of the cluster system and the total number of globular clusters (Fig 14 of Lim et al. 2024), and here the VCC 615 system presents as quite large, nearly 2.5 times the size predicted by the  $R_{e,GC}-N_{GC,tot}$  relationship. This combination — relatively normal in  $R_{e,GC}/R_{e,*}$  ratio but high in  $R_{e,GC}/N_{GC,tot}$  ratio — may be a sign that the processes that led to the galaxy being large for its luminosity (i.e., ultradiffuse) may also have led to a globular cluster system large for its total population. Whether these properties were imprinted early, as the galaxy formed, or are a result of ongoing evolution in the cluster environment remains unclear.

## 6. VCC 615'S OFFSET NUCLEUS

The brightest compact source in VCC 615 is the galaxy's offset nucleus, projected just  $3.4''$  (290 pc, or  $0.13 R_{e,*}$ ) northeast of the galaxy's isophotal center. The nucleus is photometrically distinct from the other cluster candidates in being significantly more luminous and somewhat redder in color (Figure 5). Surrounding the nucleus is a diffuse but semi-resolved envelope of starlight which proved difficult to fit using *galfit*; despite many different trials, we were unable to achieve a fully converged model in either the F814W or F475W imaging. In both cases, the fits yielded large values for Sérsic- $n$  (10.3 and 13.5 in F475W and F814W, respectively), much larger than the typical values for our cluster candidates ( $n \approx 1 - 5$ ). These larger values for Sérsic- $n$  are qualitatively consistent with the presence of an extended envelope, and attempts to re-fit the nucleus with a more globular-like Sérsic- $n = 5$  yielded significantly worse residuals. We infer that the larger  $n$

values are necessary to fit this source, even if the exact value is not well-determined. However, despite this uncertainty of the `galfit` modeling, the object’s fitted half-light radius was quite consistent in both bands, with  $R_{h,F475W} = 0.16'' \pm 0.01''$  and  $R_{h,F814W} = 0.17'' \pm 0.01''$ .

The high luminosity ( $M_{F814W} = -11.4$ ), large size ( $R_h = 14$  pc), and high Sérsic- $n$  of this source make it unlike our other globular cluster candidates and more like a bona-fide nucleus. In Virgo, the nucleation fraction for galaxies of similar stellar mass to VCC 615 ( $\log M_* = 7.86$ , Roediger et al. in prep) is  $\sim 60\%$  (Sánchez-Janssen et al. 2019), so it is unsurprising for the galaxy to be nucleated. However, offset nuclei are more rare: Binggeli et al. (2000) estimate that only 20% of Virgo dE,N galaxies have offset nuclei, with a weak trend for the offset to be larger for galaxies at lower surface brightness (see also Poulain et al. 2021; Lambert et al. 2024). In some cases, these may be chance projections of a compact source (a UCD or massive globular cluster) onto the face of the galaxy, but that is unlikely the case here. Not only is the nucleus projected only  $3.4''$  from the center, it also has a radial velocity that is only  $4 \text{ km s}^{-1}$  different from VCC 615’s systemic velocity measured by Toloba et al. (2023).

So what has caused the nucleus to be offset in VCC 615? One possibility is that tidal encounters in the Virgo environment have perturbed the galaxy such that the isophotal center itself is misplaced. This, too, appears unlikely: the galaxy shows no sign of isophotal irregularity in ground based imaging by the NGVS (Ferrarese et al. 2012) or the Burrell Schmidt Deep Virgo Survey (Mihos et al. 2017) projects, and the spatial distribution of galaxy’s resolved stellar populations appears quite round and symmetric to even lower equivalent surface brightness as well (Mihos et al. 2022).

A more speculative possibility is that we are seeing the result of recent mergers of globular clusters to form the nucleus. If UDGs are embedded in massive dark halos, dynamical friction will be particularly efficient at driving globular clusters to the center of the galaxy (Lotz et al. 2001; Dutta Chowdhury et al. 2020; Bar et al. 2022) where they may merge to form luminous nuclei, similar to scenarios proposed in normal galaxies (e.g., Tremaine et al. 1975; Gnedin et al. 2014; Arca-Sedda & Capuzzo-Dolcetta 2014). Certainly in the case of VCC 615, both the dynamical mass estimate (Toloba et al. 2023) and the high globular cluster specific frequency argue for such a massive dark halo. Under this scenario, the nucleus being offset from the center may just be a sign that this sinking process has not completely finished, or that the central potential is shallow enough that the nucleus can oscillate around the core

for an extended period of time (Miller & Smith 1992; Taga & Iye 1998).

Regardless of the origin of the nucleus, its overall properties make it similar to the population of UCDs found within the Virgo cluster. These UCDs are typically larger and much more luminous than most globular clusters (e.g., Jones et al. 2006; Brodie et al. 2011; Chiboucas et al. 2011; Liu et al. 2015, 2020, and references therein), and a number of UCDs have been found to be embedded in faint and diffuse envelopes (e.g., Liu et al. 2015; Vogel et al. 2016; Wang et al. 2023), qualitatively similar to the extended light that gives rise to the high Sérsic- $n$  value we infer when fitting this source. If this central source is indeed a nucleus, we may be seeing the first steps of the evolutionary stripping process outlined by Wang et al. (2023), wherein VCC 615 is slowly being stripped by gravitational tides in the Virgo Cluster, and may ultimately lead to the total destruction of the main galaxy leaving behind the nucleus as a Virgo UCD.

## 7. SUMMARY

We have used F475W and F814W imaging from the ACS camera on the *Hubble Space Telescope* to study the globular cluster system of the Virgo Cluster ultra-diffuse galaxy VCC 615. Our *Hubble* imaging lets us construct a very clean and deep sample of globular cluster candidates that extends more than 90% down the globular cluster luminosity function, while simultaneously rejecting background galaxies that would be unresolved contaminants in ground-based imaging. We follow up the globular cluster selection by measuring the half-light radii of the cluster candidates using the image analysis package `galfit` (Peng et al. 2010). Using the photometry and size measurements of the cluster candidates, along with a well-determined TRGB distance for the galaxy, (Mihos et al. 2022), we are able to accurately characterize the physical properties of both the galaxy’s globular cluster system and its offset nucleus. We compare the properties of the VCC 615 globular cluster system to those of other UDGs, as well as to those in galaxies more broadly. Our most important results are as follows:

1. After selecting on a combination of F475W–F814W color, source size as measured by 3- and 6-pixel aperture magnitudes, and (for brighter sources) ground-based  $u^*$ ,  $g'$ ,  $i'$  imaging, we identify 23 globular cluster candidates in the ACS field of view, down to a limiting magnitude (set by confusion with background sources) of F814W=24.0. Of these sources, 15 are located within 1.5 half-light radii of the center of the galaxy, including the galaxy’s compact nucleus.

This nucleus is both photometrically and structurally distinct from the other cluster candidates, and is removed from our sample to be considered separately.

2. Using `galfit` we are able to measure half-light radii down to  $R_h = 0.015''$  (1.3 pc). Of the 22 globular cluster candidates, 6 are unresolved, while the other 16 have well-determined half-light radii spanning the range 2–17 pc. The resolved sources are almost equally split between objects with half-light radii in the range 2–8 pc, similar to many Galactic globular clusters, and those with much larger half-light radii in the range 9–17 pc. These latter sources comprise 32% (7/22) of the total sample of globular cluster candidates and seem more akin to the “extended star clusters” (ESCs) found around a number of nearby galaxies. Of these 7 large cluster candidates, three are spectroscopically confirmed to be in Virgo [Toloba et al. \(2023\)](#), while two others are located very near the center of the galaxy (at  $R < 0.5R_{e,*}$ ). Thus the likelihood that this population of sources is contaminants is very small.
3. The luminosity function of the globular clusters in VCC 615 is characterized by a log normal distribution with a peak magnitude of F814W =  $22.78_{-0.22}^{+0.39}$  ( $M_{F814W} = -8.45$  at the 17.7 Mpc distance of VCC 615) and width  $\sigma = 0.86_{-0.19}^{+0.37}$ . The GCLF width is consistent with that derived more broadly for galaxies similar in luminosity to VCC 615, and while the GCLF peak magnitude appears slightly brighter (by  $\approx 0.3$  mag) than expected, we see no evidence for a population of extremely over-luminous globular clusters as has been reported in some other UDGs.
4. The globular clusters have a mean color of F475W–F814W = 1.40, characteristic of metal-poor stellar populations, and we find no clusters redder than F475W–F814W = 1.5. The dispersion in color is small  $\sigma = 0.06$  mag, but not as anomalously monochromatic as the cluster systems found in some other UDG systems.
5. We derive a total globular cluster count for VCC 615 of  $N_{GC} = 25.1_{-5.4}^{+6.5}$ , after accounting for spatial and photometric incompleteness. This yields a globular cluster specific frequency of  $S_N = 55.5_{-12.0}^{+14.5}$  which is quite large compared to typical dwarf galaxies of VCC 615’s luminosity and implies a large mass-to-light ratio for the galaxy. Using the scaling relationships between globular

cluster count and total galaxy mass from [Harris et al. \(2017\)](#), we derive a total mass for VCC 615 in the range of  $M_{tot} = 0.9 - 1.6 \times 10^{11} M_{\odot}$ , yielding a ratio of stellar mass to halo mass of  $\log(M_*/M_h) \approx -3.1$ . This value is lower than that predicted by models of the stellar mass – halo mass relationship (e.g., [Behroozi et al. 2013](#); [Moster et al. 2013](#)), and provides independent confirmation of the galaxy’s high mass-to-light ratio as derived from the kinematics of its globular cluster system ([Toloba et al. 2018, 2023](#)).

6. VCC 615’s offset nucleus appears photometrically and structurally distinct from the globular cluster population, and has properties more akin to those of UCDs. The small offset between the nucleus and the photometric center of the galaxy ( $3.4''$  or  $0.13R_{e,*}$ ) suggests that the galaxy is not fully in equilibrium, and we may be seeing a nucleus recently formed from globular cluster mergers but not yet dynamically settled into the center of the galaxy.

Our study adds to the growing census of globular cluster systems in UDGs. In VCC 615, this census points to a UDG embedded in a massive dark halo which may guard the galaxy against rapid destruction by the tidal field of the Virgo Cluster. Instead, slow stripping by repeated passages through the cluster core may gradually whittle down the galaxy’s already diffuse stellar population, leaving behind only its nucleus to live on in the cluster as a UCD. The globular clusters themselves show no sign of being dramatically over-luminous or monochromatic, as has been found in some other UDGs. However, our size measurements show that VCC 615 hosts a number of very large globular clusters with half-light radii  $R_h > 9$  pc, adding to the variety of peculiar properties found in the globular cluster systems of UDGs. The frequency that these globular cluster anomalies occur, and their connection to the formation and evolution of UDGs, remains an open question.

#### ACKNOWLEDGMENTS

We thank Jay Anderson with help and suggestions regarding slightly trailed *Hubble* images. This research is based on observations made with the NASA/ESA Hubble Space Telescope for program #GO-15258 and obtained at the Space Telescope Science Institute (STScI). STScI is operated by the Association of Universities for Research in Astronomy, Inc., under NASA contract NAS5-26555. Support for this program was provided by NASA through grants to J.C.M. and P.R.D. from STScI. E.T. is thankful for support from HST GO-



15417 and NSF AST-2206498. S.L. acknowledges the support from the Sejong Science Fellowship Program by the National Research Foundation of Korea (NRF) grant funded by the Korea government (MSIT) (No. NRF-2021R1C1C2006790). This research made use of Photutils, an Astropy package for detection and photometry of astronomical sources (Bradley et al. 2023).

*Facility:* HST (ACS), CFHT (MegaCam) The Hubble Space Telescope imaging data used in this study were obtained from the Mikulski Archive for Space Telescopes (MAST) at the Space Telescope Science Institute and can be accessed via DOI: 10.17909/z91h-8a19.

*Software:* astropy (Astropy Collaboration et al. 2013, 2018, 2022), emcee (Foreman-Mackey et al. 2019), galfit (Peng et al. 2010) numpy (Harris et al. 2020), matplotlib (Hunter et al. 2007), photutils (Bradley et al. 2023), scipy (Virtanen et al. 2020),

## REFERENCES

- Astropy Collaboration, Robitaille, T. P., Tollerud, E. J., et al. 2013, *A&A*, 558, A33.  
doi:10.1051/0004-6361/201322068
- Astropy Collaboration, Price-Whelan, A. M., Sipőcz, B. M., et al. 2018, *AJ*, 156, 123. doi:10.3847/1538-3881/aabc4f
- Astropy Collaboration, Price-Whelan, A. M., Lim, P. L., et al. 2022, *ApJ*, 935, 167. doi:10.3847/1538-4357/ac7c74
- Amorisco, N. C. & Loeb, A. 2016, *MNRAS*, 459, L51.  
doi:10.1093/mnrasl/slw055
- Amorisco, N. C., Monachesi, A., Agnello, A., et al. 2018, *MNRAS*, 475, 4235. doi:10.1093/mnras/sty116
- Arca-Sedda, M. & Capuzzo-Dolcetta, R. 2014, *MNRAS*, 444, 3738. doi:10.1093/mnras/stu1683
- Bar, N., Danieli, S., & Blum, K. 2022, *ApJL*, 932, L10.  
doi:10.3847/2041-8213/ac70df
- Barbosa, C. E., Zaritsky, D., Donnerstein, R., et al. 2020, *ApJS*, 247, 46. doi:10.3847/1538-4365/ab7660
- Baumgardt, H. & Vasiliev, E. 2021, *MNRAS*, 505, 5957.  
doi:10.1093/mnras/stab1474
- Baumgardt, H., Sollima, A., Hilker, M. et al. 2023, Fundamental parameters of Galactic clusters, <https://people.smp.uq.edu.au/HolgerBaumgardt/globular/>
- Beasley, M. A. & Trujillo, I. 2016, *ApJ*, 830, 23.  
doi:10.3847/0004-637X/830/1/23
- Beasley, M. A., Romanowsky, A. J., Pota, V., et al. 2016, *ApJL*, 819, L20. doi:10.3847/2041-8205/819/2/L20
- Behroozi, P. S., Conroy, C., & Wechsler, R. H. 2010, *ApJ*, 717, 379. doi:10.1088/0004-637X/717/1/379
- Behroozi, P. S., Wechsler, R. H., & Conroy, C. 2013, *ApJ*, 770, 57. doi:10.1088/0004-637X/770/1/57
- Bekki, K., Couch, W. J., Drinkwater, M. J., et al. 2003, *MNRAS*, 344, 399. doi:10.1046/j.1365-8711.2003.06916.x
- Benavides, J. A., Sales, L. V., Abadi, M. G., et al. 2023, *MNRAS*, 522, 1033. doi:10.1093/mnras/stad1053
- Binggeli, B., Tammann, G. A., & Sandage, A. 1987, *AJ*, 94, 251. doi:10.1086/114467
- Binggeli, B., Barazza, F., & Jerjen, H. 2000, *A&A*, 359, 447
- Blakeslee, J. P. 1997, *ApJL*, 481, L59. doi:10.1086/310653
- Blakeslee, J. P., Tonry, J. L., & Metzger, M. R. 1997, *AJ*, 114, 482. doi:10.1086/118488
- Blakeslee, J. P., Jordán, A., Mei, S., et al. 2009, *ApJ*, 694, 556. doi:10.1088/0004-637X/694/1/556
- Bohlin, R. C. 2016, *AJ*, 152, 60.  
doi:10.3847/0004-6256/152/3/60
- Bradley, L., Sipőcz, B., Robitaille, T., et al. 2023, Zenodo
- Brodie, J. P., Romanowsky, A. J., Strader, J., et al. 2011, *AJ*, 142, 199. doi:10.1088/0004-6256/142/6/199
- Burkert, A. & Forbes, D. A. 2020, *AJ*, 159, 56.  
doi:10.3847/1538-3881/ab5b0e
- Cannon, J. M., Martinkus, C. P., Leisman, L., et al. 2015, *AJ*, 149, 72. doi:10.1088/0004-6256/149/2/72
- Cantiello, M., Blakeslee, J. P., Ferrarese, L., et al. 2024, *ApJ*, 966, 145. doi:10.3847/1538-4357/ad3453
- Carleton, T., Errani, R., Cooper, M., et al. 2019, *MNRAS*, 485, 382. doi:10.1093/mnras/stz383
- Chandar, R., Whitmore, B., & Lee, M. G. 2004, *ApJ*, 611, 220. doi:10.1086/421934
- Chiboucas, K., Tully, R. B., Marzke, R. O., et al. 2011, *ApJ*, 737, 86. doi:10.1088/0004-637X/737/2/86
- Chilingarian, I. V., Afanasiev, A. V., Grishin, K. A., et al. 2019, *ApJ*, 884, 79. doi:10.3847/1538-4357/ab4205
- Cho, H., Blakeslee, J. P., Chies-Santos, A. L., et al. 2016, *ApJ*, 822, 95. doi:10.3847/0004-637X/822/2/95
- Cole, A. A., Weisz, D. R., Skillman, E. D., et al. 2017, *ApJ*, 837, 54. doi:10.3847/1538-4357/aa5dff6
- Da Costa, G. S., Grebel, E. K., Jerjen, H., et al. 2009, *AJ*, 137, 4361. doi:10.1088/0004-6256/137/5/4361
- Danieli, S., van Dokkum, P., Conroy, C., et al. 2019, *ApJL*, 874, L12. doi:10.3847/2041-8213/ab0e8c
- Danieli, S., van Dokkum, P., Trujillo-Gomez, S., et al. 2022, *ApJL*, 927, L28. doi:10.3847/2041-8213/ac590a
- Di Cintio, A., Brook, C. B., Dutton, A. A., et al. 2017, *MNRAS*, 466, L1. doi:10.1093/mnrasl/slw210

- Durrell, P. R., Harris, W. E., Geisler, D., et al. 1996, *AJ*, 112, 972. doi:10.1086/118071
- Durrell, P. R., Côté, P., Peng, E. W., et al. 2014, *ApJ*, 794, 103. doi:10.1088/0004-637X/794/2/103
- Dutta Chowdhury, D., van den Bosch, F. C., & van Dokkum, P. 2020, *ApJ*, 903, 149. doi:10.3847/1538-4357/abb947
- Dutton, A. A. & Macciò, A. V. 2014, *MNRAS*, 441, 3359. doi:10.1093/mnras/stu742
- Ferrarese, L., Côté, P., Cuillandre, J.-C., et al. 2012, *ApJS*, 200, 4. doi:10.1088/0067-0049/200/1/4
- Ferrarese, L., Côté, P., MacArthur, L. A., et al. 2020, *ApJ*, 890, 128. doi:10.3847/1538-4357/ab339f
- Fielder, C. E., Jones, M. G., Sand, D. J., et al. 2023, *ApJL*, 954, L39. doi:10.3847/2041-8213/acf0c3
- Forbes, D. A., Pota, V., Usher, C., et al. 2013, *MNRAS*, 435, L6. doi:10.1093/mnrasl/slt078
- Forbes, D. A., Alabi, A., Romanowsky, A. J., et al. 2020, *MNRAS*, 492, 4874. doi:10.1093/mnras/staa180
- Forbes, D. A., Gannon, J. S., Romanowsky, A. J., et al. 2021, *MNRAS*, 500, 1279. doi:10.1093/mnras/staa3289
- Forbes, D. A. & Gannon, J. 2024, *MNRAS*, 528, 608. doi:10.1093/mnras/stad4004
- Foreman-Mackey, D., Farr, W., Sinha, M., et al. 2019, *The Journal of Open Source Software*, 4, 1864. doi:10.21105/joss.01864
- Gnedin, O. Y., Ostriker, J. P., & Tremaine, S. 2014, *ApJ*, 785, 71. doi:10.1088/0004-637X/785/1/71
- Georgiev, I. Y., Puzia, T. H., Hilker, M., et al. 2009, *MNRAS*, 392, 879. doi:10.1111/j.1365-2966.2008.14104.x
- Georgiev, I. Y., Puzia, T. H., Goudfrooij, P., et al. 2010, *MNRAS*, 406, 1967. doi:10.1111/j.1365-2966.2010.16802.x
- Harris, W. E. & van den Bergh, S. 1981, *AJ*, 86, 1627. doi:10.1086/113047
- Harris, W. E. 1996, *AJ*, 112, 1487. doi:10.1086/118116
- Harris, W. E. 2009, *ApJ*, 699, 254. doi:10.1088/0004-637X/699/1/254
- Harris, W. E. 2023, *ApJS*, 265, 9. doi:10.3847/1538-4365/acab5c
- Harris, W. E., Whitmore, B. C., Karakla, D., et al. 2006, *ApJ*, 636, 90. doi:10.1086/498058
- Harris, W. E., Harris, G. L. H., & Alessi, M. 2013, *ApJ*, 772, 82. doi:10.1088/0004-637X/772/2/82
- Harris, W. E., Blakeslee, J. P., & Harris, G. L. H. 2017, *ApJ*, 836, 67. doi:10.3847/1538-4357/836/1/67
- Harris, C.R., Millman, K.J., van der Walt, S.J. et al. 2020, *Nature*, 585, 357
- Harris, W. E., Brown, R. A., Durrell, P. R., et al. 2020, *ApJ*, 890, 105. doi:10.3847/1538-4357/ab6992
- Harris, W. E. & van den Bergh, S. 1981, *AJ*, 86, 1627. doi:10.1086/113047
- Hudson, M. J., Harris, G. L., & Harris, W. E. 2014, *ApJL*, 787, L5. doi:10.1088/2041-8205/787/1/L5
- Hunter, J.D., 2007, *Computing in Science and Engineering*, 9:3, 90.
- Hurley, J. R. & Mackey, A. D. 2010, *MNRAS*, 408, 2353. doi:10.1111/j.1365-2966.2010.17285.x
- Huxor, A. P., Tanvir, N. R., Irwin, M. J., et al. 2005, *MNRAS*, 360, 1007. doi:10.1111/j.1365-2966.2005.09086.x
- Huxor, A. P., Mackey, A. D., Ferguson, A. M. N., et al. 2014, *MNRAS*, 442, 2165. doi:10.1093/mnras/stu771
- Hwang, N., Lee, M. G., Lee, J. C., et al. 2011, *ApJ*, 738, 58. doi:10.1088/0004-637X/738/1/58
- Janssens, S. R., Abraham, R., Brodie, J., et al. 2019, *ApJ*, 887, 92. doi:10.3847/1538-4357/ab536c
- Janssens, S. R., Romanowsky, A. J., Abraham, R., et al. 2022, *MNRAS*, 517, 858. doi:10.1093/mnras/stac2717
- Jones, J. B., Drinkwater, M. J., Jurek, R., et al. 2006, *AJ*, 131, 312. doi:10.1086/497960
- Jordán, A., Côté, P., Blakeslee, J. P., et al. 2005, *ApJ*, 634, 1002. doi:10.1086/497092
- Jordán, A., McLaughlin, D. E., Côté, P., et al. 2006, *ApJL*, 651, L25. doi:10.1086/509119
- Jordán, A., McLaughlin, D. E., Côté, P., et al. 2007, *ApJS*, 171, 101. doi:10.1086/516840
- Jordán, A., Peng, E. W., Blakeslee, J. P., et al. 2009, *ApJS*, 180, 54. doi:10.1088/0067-0049/180/1/54
- Karim, N., Collins, M. L. M., Forbes, D. A., et al. 2024, *MNRAS*, 530, 4936. doi:10.1093/mnras/stae611
- King, I. R. 1966, *AJ*, 71, 64. doi:10.1086/109857
- Kundu, A. & Whitmore, B. C. 2001, *AJ*, 121, 2950. doi:10.1086/321073
- Lambert, M., Khim, D. J., Zaritsky, D., et al. 2024, *AJ*, 167, 61. doi:10.3847/1538-3881/ad0f25
- Larsen, S. S. 1999, *A&AS*, 139, 393. doi:10.1051/aas:1999509
- Larsen, S. S. & Brodie, J. P. 2000, *AJ*, 120, 2938. doi:10.1086/316847
- Larsen, S. S., Brodie, J. P., Huchra, J. P., et al. 2001, *AJ*, 121, 2974. doi:10.1086/321081
- Lee, M. G., Park, H. S., Kim, E., et al. 2008, *ApJ*, 682, 135. doi:10.1086/587469
- Leisman, L., Haynes, M. P., Janowiecki, S., et al. 2017, *ApJ*, 842, 133. doi:10.3847/1538-4357/aa7575
- Liao, S., Gao, L., Frenk, C. S., et al. 2019, *MNRAS*, 490, 5182. doi:10.1093/mnras/stz2969
- Lim, S., Peng, E. W., Duc, P.-A., et al. 2017, *ApJ*, 835, 123. doi:10.3847/1538-4357/835/2/123

- Lim, S., Peng, E. W., Côté, P., et al. 2018, *ApJ*, 862, 82.  
doi:10.3847/1538-4357/aac81
- Lim, S., Côté, P., Peng, E. W., et al. 2020, *ApJ*, 899, 69.  
doi:10.3847/1538-4357/aba433
- Lim, S., Peng, E. W., Côté, P., et al. 2024, *ApJ*, 966, 168.  
doi:10.3847/1538-4357/ad3444
- Liu, C., Peng, E. W., Côté, P., et al. 2015, *ApJ*, 812, 34.  
doi:10.1088/0004-637X/812/1/34
- Liu, Y., Peng, E. W., Lim, S., et al. 2016, *ApJ*, 830, 99.  
doi:10.3847/0004-637X/830/2/99
- Liu, C., Côté, P., Peng, E. W., et al. 2020, *ApJS*, 250, 17.  
doi:10.3847/1538-4365/abad91
- Longobardi, A., Peng, E. W., Côté, P., et al. 2018, *ApJ*, 864, 36. doi:10.3847/1538-4357/aad3d2
- Lotz, J. M., Telford, R., Ferguson, H. C., et al. 2001, *ApJ*, 552, 572. doi:10.1086/320545
- Lotz, J. M., Miller, B. W., & Ferguson, H. C. 2004, *ApJ*, 613, 262. doi:10.1086/422871
- Ma, J., Wang, S., Wang, S., et al. 2020, *MNRAS*, 496, 3741. doi:10.1093/mnras/staa1775
- Mackey, A. D. & van den Bergh, S. 2005, *MNRAS*, 360, 631. doi:10.1111/j.1365-2966.2005.09080.x
- Mackey, A. D., Ferguson, A. M. N., Huxor, A. P., et al. 2019, *MNRAS*, 484, 1756. doi:10.1093/mnras/stz072
- Madrid, J. P., Harris, W. E., Blakeslee, J. P., et al. 2009, *ApJ*, 705, 237. doi:10.1088/0004-637X/705/1/237
- Marleau, F. R., Habas, R., Poulain, M., et al. 2021, *A&A*, 654, A105. doi:10.1051/0004-6361/202141432
- Marleau, F. R., Duc, P.-A., Poulain, M., et al. 2024, arXiv:2408.03311. doi:10.48550/arXiv.2408.03311
- Mei, S., Blakeslee, J. P., Côté, P., et al. 2007, *ApJ*, 655, 144. doi:10.1086/509598
- Mihos, J. C., Harding, P., Feldmeier, J. J., et al. 2017, *ApJ*, 834, 16. doi:10.3847/1538-4357/834/1/16
- Mihos, J. C., Carr, C. T., Watkins, A. E., et al. 2018, *ApJL*, 863, L7. doi:10.3847/2041-8213/aad62e
- Mihos, J. C., Durrell, P. R., Ferrarese, L., et al. 2015, *ApJL*, 809, L21. doi:10.1088/2041-8205/809/2/L21
- Mihos, J. C., Durrell, P. R., Toloba, E., et al. 2022, *ApJ*, 924, 87. doi:10.3847/1538-4357/ac35d9
- Miller, B. W. & Lotz, J. M. 2007, *ApJ*, 670, 1074. doi:10.1086/522323
- Miller, R. H. & Smith, B. F. 1992, *ApJ*, 393, 508. doi:10.1086/171523
- Moore, B., Katz, N., Lake, G., et al. 1996, *Nature*, 379, 613. doi:10.1038/379613a0
- Moster, B. P., Naab, T., & White, S. D. M. 2013, *MNRAS*, 428, 3121. doi:10.1093/mnras/sts261
- Müller, O., Durrell, P. R., Marleau, F. R., et al. 2021, *ApJ*, 923, 9. doi:10.3847/1538-4357/ac2831
- Muñoz, R. P., Puzia, T. H., Lançon, A., et al. 2014, *ApJS*, 210, 4. doi:10.1088/0067-0049/210/1/4
- Navarro, J. F., Frenk, C. S., & White, S. D. M. 1997, *ApJ*, 490, 493. doi:10.1086/304888
- Peng, E. W., Côté, P., Jordán, A., et al. 2006, *ApJ*, 639, 838. doi:10.1086/499485
- Peng, E. W., Jordán, A., Blakeslee, J. P., et al. 2009, *ApJ*, 703, 42. doi:10.1088/0004-637X/703/1/42
- Peng, E. W., Jordán, A., Côté, P., et al. 2008, *ApJ*, 681, 197. doi:10.1086/587951
- Peng, C. Y., Ho, L. C., Impey, C. D., et al. 2010, *AJ*, 139, 2097. doi:10.1088/0004-6256/139/6/2097
- Peng, E. W., Ferguson, H. C., Goudfrooij, P., et al. 2011, *ApJ*, 730, 23. doi:10.1088/0004-637X/730/1/23
- Peng, E. W. & Lim, S. 2016, *ApJL*, 822, L31. doi:10.3847/2041-8205/822/2/L31
- Pfeffer, J. & Baumgardt, H. 2013, *MNRAS*, 433, 1997. doi:10.1093/mnras/stt867
- Poulain, M., Marleau, F. R., Habas, R., et al. 2021, *MNRAS*, 506, 5494. doi:10.1093/mnras/stab2092
- Prole, D. J., Hilker, M., van der Burg, R. F. J., et al. 2019, *MNRAS*, 484, 4865. doi:10.1093/mnras/stz326
- Puzia, T. H., Paolillo, M., Goudfrooij, P., et al. 2014, *ApJ*, 786, 78. doi:10.1088/0004-637X/786/2/78
- Roediger, J. et al., in prep
- Romanowsky, A. J., Larsen, S. S., Villaume, A., et al. 2023, *MNRAS*, 518, 3164. doi:10.1093/mnras/stac2898
- Saifollahi, T., Trujillo, I., Beasley, M. A., et al. 2021, *MNRAS*, 502, 5921. doi:10.1093/mnras/staa3016
- Saifollahi, T., Zaritsky, D., Trujillo, I., et al. 2022, *MNRAS*, 511, 4633. doi:10.1093/mnras/stac328
- Sánchez-Janssen, R., Côté, P., Ferrarese, L., et al. 2019, *ApJ*, 878, 18. doi:10.3847/1538-4357/aaf4fd
- Sandage, A. & Binggeli, B. 1984, *AJ*, 89, 919. doi:10.1086/113588
- Schlafly, E. F. & Finkbeiner, D. P. 2011, *ApJ*, 737, 103. doi:10.1088/0004-637X/737/2/103
- Sharina, M. E., Puzia, T. H., & Makarov, D. I. 2005, *A&A*, 442, 85. doi:10.1051/0004-6361:20052921
- Shen, Z., Danieli, S., van Dokkum, P., et al. 2021, *ApJL*, 914, L12. doi:10.3847/2041-8213/ac0335
- Shen, Z., van Dokkum, P., & Danieli, S. 2021, *ApJ*, 909, 179. doi:10.3847/1538-4357/abdd29
- Spitler, L. R. & Forbes, D. A. 2009, *MNRAS*, 392, L1. doi:10.1111/j.1745-3933.2008.00567.x
- Strader, J., Brodie, J. P., Spitler, L., et al. 2006, *AJ*, 132, 2333. doi:10.1086/509124
- Taga, M. & Iye, M. 1998, *MNRAS*, 299, 111. doi:10.1046/j.1365-8711.1998.01753.x

- Toloba, E., Lim, S., Peng, E., et al. 2018, *ApJL*, 856, L31. doi:10.3847/2041-8213/aab603
- Toloba, E., Sales, L. V., Lim, S., et al. 2023, *ApJ*, 951, 77. doi:10.3847/1538-4357/acd336
- Tremaine, S. D., Ostriker, J. P., & Spitzer, L. 1975, *ApJ*, 196, 407. doi:10.1086/153422
- Trujillo, I., Beasley, M. A., Borlaff, A., et al. 2019, *MNRAS*, 486, 1192. doi:10.1093/mnras/stz771
- van Dokkum, P., Danieli, S., Abraham, R., et al. 2019, *ApJL*, 874, L5. doi:10.3847/2041-8213/ab0d92
- van Dokkum, P., Abraham, R., Romanowsky, A. J., et al. 2017, *ApJL*, 844, L11. doi:10.3847/2041-8213/aa7ca2
- van Dokkum, P., Danieli, S., Cohen, Y., et al. 2018, *Nature*, 555, 629. doi:10.1038/nature25767
- van Dokkum, P., Cohen, Y., Danieli, S., et al. 2018, *ApJL*, 856, L30. doi:10.3847/2041-8213/aab60b
- van Dokkum, P., Abraham, R., Brodie, J., et al. 2016, *ApJL*, 828, L6. doi:10.3847/2041-8205/828/1/L6
- van Dokkum, P. G., Abraham, R., Merritt, A., et al. 2015, *ApJL*, 798, L45. doi:10.1088/2041-8205/798/2/L45
- van Dokkum, P., Shen, Z., Romanowsky, A. J., et al. 2022, *ApJL*, 940, L9. doi:10.3847/2041-8213/ac94d6
- Villegas, D., Jordán, A., Peng, E. W., et al. 2010, *ApJ*, 717, 603. doi:10.1088/0004-637X/717/2/603
- Virtanen, P., Gommers, R., Oliphant, T. E. et al. 2020, *Nature Methods*, 17, 261
- Voggel, K., Hilker, M., & Richtler, T. 2016, *A&A*, 586, A102. doi:10.1051/0004-6361/201527070
- Wang, K., Peng, E. W., Liu, C., et al. 2023, *Nature*, 623, 296. doi:10.1038/s41586-023-06650-z
- Zaritsky, D. 2022, *MNRAS*, 513, 2609. doi:10.1093/mnras/stac1072
- Zaritsky, D., Donnerstein, R., Dey, A., et al. 2023, *ApJS*, 267, 27. doi:10.3847/1538-4365/acdd71

**Table 3.** VCC 615 Globular Cluster Candidates

| Obj ID  | RA<br>(J2000) | Dec<br>(J2000) | F814W        | F475W–F814W | $R_h$<br>(arcsec) | $(b/a)$ | $M_{F814W}$ | $R_h$<br>(pc) | Velocity<br>(km s <sup>-1</sup> ) |
|---------|---------------|----------------|--------------|-------------|-------------------|---------|-------------|---------------|-----------------------------------|
| Nucleus | 185.769724    | 12.015569      | 19.85 ± 0.01 | 1.50 ± 0.01 | [0.167 ± 0.003]   | [0.79]  | -11.39      | [14.4]        | 2094 ± 4                          |
| GC01    | 185.762994    | 12.007492      | 21.35 ± 0.02 | 1.32 ± 0.01 | 0.053 ± 0.001     | 0.57    | -9.89       | 4.5           | 2091 ± 12                         |
| GC02    | 185.776776    | 12.016368      | 21.40 ± 0.01 | 1.36 ± 0.01 | [0.035 ± 0.001]   | [0.91]  | -9.84       | [3.0]         | 2122 ± 15                         |
| GC03    | 185.761882    | 12.011469      | 21.99 ± 0.02 | 1.45 ± 0.01 | 0.077 ± 0.003     | 0.85    | -9.25       | 6.6           | —                                 |
| GC04    | 185.774964    | 12.021906      | 22.02 ± 0.02 | 1.29 ± 0.01 | 0.049 ± 0.001     | 0.89    | -9.22       | 4.2           | 2075 ± 7                          |
| GC05    | 185.757501    | 11.994417      | 22.05 ± 0.02 | 1.33 ± 0.02 | 0.060 ± 0.001     | 0.89    | -9.19       | 5.2           | 2099 ± 12                         |
| GC06    | 185.769535    | 12.016412      | 22.07 ± 0.04 | 1.40 ± 0.02 | 0.144 ± 0.012     | 0.83    | -9.17       | 12.3          | —                                 |
| GC07    | 185.785027    | 12.017800      | 22.24 ± 0.03 | 1.38 ± 0.02 | 0.128 ± 0.006     | 0.87    | -9.00       | 11.0          | 2169 ± 33                         |
| GC08    | 185.770645    | 12.016551      | 22.32 ± 0.02 | 1.31 ± 0.02 | 0.046 ± 0.001     | 0.91    | -8.92       | 3.9           | 2119 ± 20                         |
| GC09    | 185.779822    | 12.024019      | 22.37 ± 0.06 | 1.33 ± 0.02 | 0.148 ± 0.014     | 0.80    | -8.87       | 12.7          | 2050 ± 18                         |
| GC10    | 185.777010    | 12.008676      | 22.37 ± 0.05 | 1.40 ± 0.02 | 0.113 ± 0.010     | 0.84    | -8.87       | 9.7           | —                                 |
| GC11    | 185.777554    | 12.021043      | 22.59 ± 0.02 | 1.32 ± 0.02 | 0.053 ± 0.001     | 0.89    | -8.65       | 4.6           | —                                 |
| GC12    | 185.769296    | 12.012033      | 22.69 ± 0.08 | 1.46 ± 0.03 | 0.173 ± 0.023     | 0.90    | -8.55       | 14.9          | 1966 ± 41                         |
| GC13    | 185.764798    | 12.015294      | 22.81 ± 0.03 | 1.40 ± 0.03 | 0.062 ± 0.004     | 0.84    | -8.43       | 5.3           | —                                 |
| GC14    | 185.758685    | 12.017551      | 22.87 ± 0.02 | 1.47 ± 0.03 | 0.043 ± 0.001     | 0.95    | -8.37       | 3.7           | —                                 |
| GC15    | 185.769262    | 12.000680      | 22.93 ± 0.03 | 1.42 ± 0.03 | [0.001 ± 0.002]   | [0.53]  | -8.39       | [0.0]         | —                                 |
| GC16    | 185.766155    | 12.014674      | 23.16 ± 0.13 | 1.42 ± 0.04 | 0.201 ± 0.041     | 0.80    | -8.08       | 17.3          | —                                 |
| GC17    | 185.740219    | 12.002410      | 23.25 ± 0.03 | 1.46 ± 0.04 | [0.001 ± 0.002]   | [0.56]  | -8.15       | [0.1]         | —                                 |
| GC18    | 185.778809    | 12.013634      | 23.28 ± 0.03 | 1.40 ± 0.04 | [0.001 ± 0.006]   | [0.08]  | -8.07       | [0.1]         | —                                 |
| GC19    | 185.775583    | 11.991292      | 23.31 ± 0.10 | 1.47 ± 0.05 | 0.114 ± 0.020     | 0.83    | -7.93       | 9.8           | —                                 |
| GC20    | 185.767108    | 12.021113      | 23.42 ± 0.03 | 1.48 ± 0.04 | [0.011 ± 0.002]   | [0.09]  | -7.80       | [1.0]         | —                                 |
| GC21    | 185.781126    | 12.002181      | 23.45 ± 0.03 | 1.43 ± 0.05 | [0.001 ± 0.001]   | [0.69]  | -7.93       | [0.0]         | —                                 |
| GC22    | 185.784051    | 12.037663      | 23.76 ± 0.03 | 1.48 ± 0.06 | [0.004 ± 0.003]   | [0.07]  | -7.58       | [0.4]         | —                                 |

NOTE—The listed F814W magnitudes are the fitted total magnitudes from `galfit`, except for unresolved objects ( $R_h < 0.015''$ ) where we list the 6-pixel aperture corrected magnitudes. The F475W–F814W Vega magnitudes for all objects are derived from the 6-pixel aperture magnitudes. The values for half-light radius ( $R_h$ ) and ellipticity ( $b/a$ ) come from the `galfit` modeling; values listed in brackets denote unconverged or unresolved fits. Absolute F814W magnitudes and physical half-light radii are derived using a distance to VCC 615 of 17.7 Mpc (Mihos et al. 2022), while velocities are taken from Toloba et al. (2023). All magnitudes and colors are corrected for Galactic extinction using values of  $A_{F475W} = 0.062$ ,  $A_{F814W} = 0.038$  (Schlafly & Finkbeiner 2011).